The Astrophysical Journal, 794:103 (20pp), 2014 October 20 doi:10.1088/0004-637X/794/2/103

THE NEXT GENERATION VIRGO CLUSTER SURVEY. VIII. THE SPATIAL DISTRIBUTION OF GLOBULAR CLUSTERS IN THE VIRGO CLUSTER

Patrick R. Durrell[1], Patrick Côté[2], Eric W. Peng[3,4], John P. Blakeslee[2], Laura Ferrarese[2], J. Christopher Mihos[5], Thomas H. Puzia[6], Ariane Lançon[7], Chengze Liu[8,9], Hongxin Zhang[3,4], Jean-Charles Cuillandre[10], Alan McConnachie[2], Andrés Jordán[6], Katharine Accetta[1], Samuel Boissier[11], Alessandro Boselli[11], Stéphane Courteau[12], Pierre-Alain Duc[13], Eric Emsellem[14,15], Stephen Gwyn[2], Simona Mei[16,17], and James E. Taylor[18]

[1] Department of Physics and Astronomy, Youngstown State University, Youngstown, OH 44555, USA
[2] Herzberg Astronomy and Astrophysics, National Research Council, 5071 West Saanich Road, Victoria, BC V9E 2E7, Canada
[3] Department of Astronomy, Peking University, Beijing 100871, China
[4] Kavli Institute for Astronomy and Astrophysics, Peking University, Beijing 100871, China
[5] Department of Astronomy, Case Western Reserve University, Cleveland, OH 44106, USA
[6] Institute of Astrophysics, Pontificia Universidad Catolica, Av. Vicu'a Mackenna 4860, Macul 7820436, Santiago, Chile
[7] Observatoire astronomique de Strasbourg, Université de Strasbourg, CNRS, UMR 7550, 11 rue de l'Université, F-67000 Strasbourg, France
[8] Center for Astronomy and Astrophysics, Department of Physics and Astronomy, Shanghai Jiao Tong University, 800 Dongchuan Road, Shanghai 200240, China
[9] Shanghai Key Lab for Particle Physics and Cosmology, Shanghai Jiao Tong University, Shanghai 200240, China
[10] Canada–France–Hawaii Telescope Corporation, Kamuela, HI 96743, USA
[11] Aix Marseille Université, CNRS, LAM (Laboratoire d'Astrophysique de Marseille) UMR 7326, F-13388 Marseille, France
[12] Department of Physics, Engineering Physics and Astronomy, Queen's University, Kingston, ON K7L 3N6, Canada
[13] AIM Paris Saclay, CNRS/INSU, CEA/Irfu, Université Paris Diderot, Orme des Merisiers, F-91191 Gif sur Yvette cedex, France
[14] Université de Lyon 1, CRAL, Observatoire de Lyon, 9 av. Charles André, F-69230 Saint-Genis Laval; CNRS, UMR 5574; ENS de Lyon, France
[15] European Southern Observatory, Karl-Schwarzschild-Strasse 2, D-85748 Garching, Germany
[16] GEPI, Observatoire de Paris, Section de Meudon, 5 Place J. Janssen, F-92190 Meudon Cedex, France
[17] Université Paris Denis Diderot, F-75205 Paris Cedex 13, France
[18] University of Waterloo, Waterloo, ON N2L 3G1, Canada
Received 2014 March 28; accepted 2014 August 9; published 2014 September 29

ABSTRACT

We report on a large-scale study of the distribution of globular clusters (GCs) throughout the Virgo cluster, based on photometry from the Next Generation Virgo Cluster Survey (NGVS), a large imaging survey covering Virgo's primary subclusters (Virgo A = M87 and Virgo B = M49) out to their virial radii. Using the g'_o, $(g' - i')_o$ color–magnitude diagram of unresolved and marginally resolved sources within the NGVS, we have constructed two-dimensional maps of the (irregular) GC distribution over 100 deg^2 to a depth of $g'_o = 24$. We present the clearest evidence to date showing the difference in concentration between red and blue GCs over the full extent of the cluster, where the red (more metal-rich) GCs are largely located around the massive early-type galaxies in Virgo, while the blue (metal-poor) GCs have a much more extended spatial distribution with significant populations still present beyond 83′ (∼215 kpc) along the major axes of both M49 and M87. A comparison of our GC maps to the diffuse light in the outermost regions of M49 and M87 show remarkable agreement in the shape, ellipticity, and boxiness of both luminous systems. We also find evidence for spatial enhancements of GCs surrounding M87 that may be indicative of recent interactions or an ongoing merger history. We compare the GC map to that of the locations of Virgo galaxies and the X-ray intracluster gas, and find generally good agreement between these various baryonic structures. We calculate the Virgo cluster contains a total population of $N_{\rm GC} = 67{,}300 \pm 14{,}400$, of which 35% are located in M87 and M49 alone. For the first time, we compute a cluster-wide specific frequency $S_{N,\rm CL} = 2.8 \pm 0.7$, after correcting for Virgo's diffuse light. We also find a GC-to-baryonic mass fraction $\epsilon_b = 5.7 \pm 1.1 \times 10^{-4}$ and a GC-to-total cluster mass formation efficiency $\epsilon_t = 2.9 \pm 0.5 \times 10^{-5}$, the latter values slightly lower than but consistent with those derived for individual galactic halos. Taken as a whole, our results show that the production of the complex structures in the unrelaxed Virgo cluster core (including the production of the diffuse intracluster light) is an ongoing and continuing process.

Key words: galaxies: clusters: general – galaxies: clusters: individual (Virgo) – galaxies: star clusters: general

Online-only material: color figures

1. INTRODUCTION

A priority in extragalactic astrophysics is to understand the hierarchical assembly of galaxy clusters, which are expected (in the ΛCDM paradigm) to have built up over time, with the larger galaxies (especially the brightest cluster galaxies; BCGs) having grown through mergers and accretion of many smaller galaxies[19] (e.g., Dubinski 1998; Springel et al. 2005; Naab et al. 2009; Ruszkowski & Springel 2009; Oser et al. 2010; Laporte et al. 2013). Thus an understanding of the mass assembly of galaxy clusters is heavily dependent on the large number of

[19] The timescales over which this happens, however, is still under debate (e.g., Collins et al. 2009).

galactic interactions that occur over the entire history of the cluster. Detailed studies of the galaxies, intracluster gas, and discrete stellar populations (i.e., stars, nebulae, star clusters) within the cluster galaxies have all provided insights into the basic framework of hierarchical evolution.

The buildup of the extended stellar halo around BCGs (and perhaps other massive cluster members) from interaction with merged/stripped galaxies also results in the formation of a much more extended envelope of stars (Dubinski 1998; Abadi et al. 2006; Rudick et al. 2006; Cypriano et al. 2006; Murante et al. 2007; Cui et al. 2014). This is the diffuse intracluster light (ICL) that is ubiquitous in massive galaxy clusters. It is comprised of stellar populations that are not gravitationally bound to any single galaxy, but are dynamically part of the galaxy cluster environment.[20] The ICL, while of extremely low surface brightness, has been studied in great detail (e.g., Feldmeier et al. 2004b; Zibetti et al. 2005; Gonzalez et al. 2005; Krick et al. 2006; Krick & Bernstein 2007; Burke et al. 2012) and is now known to contain a significant fraction of the total optical luminosity of galaxy clusters (∼10%–30%; see references above); similar fractions are predicted in theoretical studies of galaxy cluster evolution (Murante et al. 2004; Willman et al. 2004; Sommer-Larsen et al. 2005; Monaco et al. 2006; Stanghellini et al. 2006; Purcell et al. 2007).

The detailed study of this extra stellar component provides a crucial glimpse into the dynamical evolution of cluster galaxies and the physical processes that shape them, including galaxy mergers, tidal stripping, cluster virialization, and even the initial conditions of cluster formation. The ICL is also a useful probe of the continuous evolution of the galaxy cluster in which it resides; although the central BCG appears to have formed much of its mass early on, the build-up of the surrounding ICL is likely a much more gradual process, with a significant fraction of it having formed since $z = 1$ (e.g., Willman et al. 2004; Murante et al. 2007; Conroy et al. 2007; Burke et al. 2012). The wealth of substructure in and around nearby galaxies suggests that the process of ICL formation continues to the present time (Mihos et al. 2005; Rudick et al. 2009).

While studies of the diffuse ICL provide insight into the evolution of galaxy clusters, the study of the *individual* stellar populations that comprise this "extra" luminosity can provide even more useful constraints on dynamical evolution. The majority of studies of the discrete stellar populations have been carried out through searches (and subsequent studies) of planetary nebulae (PNe; e.g., Feldmeier et al. 1998, 2004a; Arnaboldi et al. 2004; Aguerri et al. 2005; Gerhard et al. 2007; Castro-Rodriguéz et al. 2009; Longobardi et al. 2013), red giant stars (Ferguson et al. 1998; Durrell et al. 2002; Williams et al. 2007a), and supernovae (Gal-Yam et al. 2003; Sand et al. 2011).

1.1. Globular Clusters

Globular clusters (GCs) provide an important tool for understanding the formation and evolution of galaxies (see the reviews by Ashman & Zepf 1998; Harris 2001; West et al. 2004; Brodie & Strader 2006). They are found in galaxies of all luminosities, environments, and Hubble types (the lone exception being the lowest luminosity dwarf galaxies with $M_V \sim -10$, which typically do not have any GCs). GCs tend to be old (∼10–12 Gyr) and have (relatively) simple stellar populations. Thus their integrated broadband optical/NIR colors can be used as a proxy for metallicity, allowing their use as tracers of the early chemical evolution of galaxies, although the form of their color–metallicity relation remains a critical issue (e.g., Puzia et al. 2002; Peng et al. 2006; Yoon et al. 2011; Blakeslee et al. 2012; Vanderbeke et al. 2014). Furthermore, GCs are the most luminous stellar systems within galaxies, allowing their visibility to greater distances than other stellar tracers—studies of GC systems extend to ∼100 Mpc and well beyond (e.g., Harris et al. 2009; West et al. 2011; Alamo-Martínez et al. 2013).

GCs are so ubiquitous that they are useful probes of not only individual galaxies, but also of the galactic environments in which they reside, from sparse galaxy groups to the densest galaxy clusters. Many studies of GC systems around galaxies have centered on the massive elliptical galaxies in dense galaxy clusters that have the largest GC populations (e.g., Harris 1986, 2009a, 2009b; Geisler et al. 1996; Blakeslee et al. 1997; Blakeslee 1999; Harris et al. 2009; Puzia et al. 2014). However, GC systems typically are quite extended and thus studies of complete GC systems around individual galaxies are difficult to carry out, especially for nearby galaxies where large area coverage is required. The availability of large CCD mosaics now enables more routine studies of not only the entire GC populations around nearby galaxies, but also *cluster-wide* GC populations.

The term "intergalactic tramp" was used in the 1950s (van den Bergh 1956, 1958; Burbidge & Sandage 1958) to describe GCs at large distances from the Milky Way (MW). However, it was the early works by Muzzio and collaborators (Forte et al. 1982; Muzzio et al. 1984; Muzzio 1986, 1987) that began to explore the scenario of "GC swapping" between galaxies in clusters. Both Muzzio (1986) and White (1987) concluded that some of these GCs would become members of the cluster itself—intracluster GCs (or IGCs). West et al. (1995) more formally developed the idea that a large IGC population could help explain the high GC specific frequency S_N values for large ellipticals in the centers of many clusters (e.g., M87 in Virgo). *N*-body simulations by Yahagi & Bekki (2005) and Bekki & Yahagi (2006) suggested—consistent with studies of intracluster stars—that IGC populations in rich clusters should comprise ∼20%–40% of the total cluster GC population.

While cluster-wide GC populations are predicted to exist, their definitive detection has been elusive, largely because of the extremely low number densities expected (thousands of GCs spread out over an entire galaxy cluster). Searches for GCs using broadband colors are necessarily statistical in nature due to a significant "background" of MW stars and distant galaxies. For example, Tamura et al. (2006a, 2006b) found that any IGC population in their study of the Virgo cluster core region would be at the $\Sigma_{GC} = 0.1$–0.5 arcmin^{-2} level, limited by background uncertainty. Bassino et al. (2003) found a spatially extended excess of objects with GC-like colors in the Fornax cluster, consistent with a cluster-wide population (also suggested by Grillmair et al. 1994; Kissler-Patig et al. 1999; Bergond et al. 2007), but follow-up spectroscopy showed that most are likely bound to NGC 1399 (Schuberth et al. 2008).

The first significant detection of a cluster-wide GC population was that by Jordán et al. (2003) in the center of A1185, later confirmed with color information by West et al. (2011). Since then, small numbers of IGCs have been confirmed in the Virgo and Fornax clusters through the visual inspection of *Hubble Space Telescope* (*HST*) images (where the GCs are resolved, and some red giant stars visible; Williams et al. 2007b) or through spectroscopy (Firth et al. 2008; Schuberth et al. 2008).

[20] While some works have differentiated between the spatially diffuse light as the ICL and the kinematically distinct populations as a "diffuse stellar component" (DSC; e.g., Dolag et al. 2010; Cui et al. 2014), we consider them both to be closely related.

The first wide-field surveys of sufficient photometric depth to detect statistically significant cluster-wide GC population were carried out in the Virgo cluster (Lee et al. 2010) and in the Coma cluster (Peng et al. 2011). Both showed a significant number of GCs outside the large galaxies of these clusters; a similar result was found with the *HST* in the much more distant cluster A1689 (Alamo-Martínez et al. 2013). Like red giant stars, GCs contain information about the metallicity and age of their parent population. Like PNe, GCs are useful tracers at very low surface densities. Like ultra-low surface brightness photometry, GC surveys can reach distances far beyond that possible via individual stars. Perhaps most importantly, GCs can serve as dynamical tracers throughout an entire cluster, making them an important yet virtually untapped resource for understanding the evolutionary states of galaxy clusters.

1.2. GCs in the Virgo Cluster

At a mean distance of 16.5 Mpc (Tonry et al. 2001; Mei et al. 2007), the Virgo Cluster provides the best laboratory for studying the formation and evolution of a typical galaxy cluster. The measured distance of the cD galaxy M87 is consistent with the cluster mean (Blakeslee et al. 2009). However, the cluster itself appears unrelaxed, and deep surface photometry of the core region around M87 by Mihos et al. (2005) clearly shows a wealth of low surface brightness streams and other diffuse features, indicative of a complex evolutionary history. Dynamical studies further showed the complexity of the M87 GC system itself (Cohen 2000; Côté et al. 2001; Strader et al. 2011; Romanowsky et al. 2012; Zhu et al. 2014). The low surface brightness features and substructure are not confined to the Virgo core but also occur around other massive galaxies and subgroups within Virgo (Janowiecki et al. 2010; Mihos et al. 2013; Paudel et al. 2013). However, the cluster's large angular extent (the photographic survey by Binggeli et al. 1985 covered a total of $\sim$140 deg^2) makes cluster-wide ICL studies extremely difficult, particularly at resolutions that allow detailed mapping at the galactic level.

Previous photometric and spectroscopic studies of GCs in Virgo have covered limited areas near individual galaxies, or larger areas to very shallow depths. However, hints of how the large-scale environment shapes galactic GC systems can be found in many of these studies. For instance, as part of the ACS Virgo Cluster Survey (ACSVCS; Côté et al. 2004), Peng et al. (2008) found that dwarf galaxies near M87 have richer GC populations than those farther out, suggesting biased GC formation. On the other hand, a possible increase of S_N (also measured from ACSVCS) for giant elliptical galaxies (excluding M87) with cluster-centric radius may be a sign of tidal stripping of the outskirts of these galaxies (Coenda et al. 2009). Lee et al. (2010) used Sloan Digital Sky Survey (SDSS) photometry to study the Virgo-wide population of GCs, but only to $i < 21.7$, at which just $\sim$13% of the complete GC population is detectable. These authors did find a statistically significant population of GCs throughout the inner regions of the Virgo Cluster, suggesting a large number of IGCs. However, the relatively low spatial resolution (limited by the small numbers of GCs detectable at SDSS depth) did not allow for a clear segregation into galactic and intracluster GC populations.

Furthermore, Virgo is a less massive, less relaxed cluster than the Coma cluster, the only other galaxy cluster in which a large-scale ($\sim$1 Mpc) study of the cluster-wide GC population has been conducted (Peng et al. 2011). Thus, an accurate census of Virgo's overall GC population would allow for useful comparisons of the intracluster stellar components in clusters of differing masses and evolutionary states. Clearly, a very deep, very wide photometric survey of the Virgo cluster has been badly needed.

1.3. The Next Generation Virgo Cluster Survey (NGVS)

The Next Generation Virgo Cluster Survey (NGVS; Ferrarese et al. 2012) is a very deep, multi-band photometric survey covering 104 deg^2 of sky in the direction of the Virgo cluster. The photometric depth of NGVS (see next section) is sufficient to reveal the majority of the GC population in Virgo. Thus, it combines the depth of some previous targeted studies (e.g., Tamura et al. 2006a, 2006b) but at twice the spatial resolution with the extremely wide field (albeit shallower) cluster-wide survey of Lee et al. (2010). The present work focuses on the search for GCs over the entire NGVS region through the use of the g'_o,$(g'-i')_o$ color–magnitude diagram (CMD) for unresolved and marginally resolved sources in the vast NGVS catalog. The exquisite data quality of the NGVS allows a thorough investigation of the amount of background contamination, the primary source of uncertainty in such studies. Other papers in the NGVS series that are related to the work presented here include spatial and kinematic studies of Virgo's ultra-compact dwarf galaxies (C. Liu et al., in preparation; H. Zhang et al., in preparation), spectroscopy of M87's GCs (E. Peng et al., in preparation), dynamical modeling of M87's GC system (Zhu et al. 2014), and the use of $u^*i'K$ imaging in the classification and detection of both stellar and galactic sources in the NGVS (Muñoz et al. 2014).

2. OBSERVATIONS AND DATA

The technical details of NGVS survey itself, including the field selection, data acquisition, and data processing are presented in Ferrarese et al. (2012), so only a brief overview will be provided here. The NGVS is a large-scale survey covering the Virgo Cluster out to one virial radius, with deep images using the Canada–France–Hawaii Telescope (CFHT) MegaCam wide-field optical imager and the $u^*g'i'z'$ filters, with partial coverage in the r' band. The MegaCam field-of-view for a single image is roughly 0.90 deg^2, although with the dithering strategy employed, the total field of view for each stacked NGVS field is $\sim$1.0 deg^2. The total NGVS survey consists of 117 separate fields and allowing for overlap between fields, the sky coverage of the NGVS is more than 104 deg^2. This covers Virgo subclusters A and B out to their virial radii. The NGVS data set also includes four separate control fields (hereafter labeled BKG1-4) that are located $\sim$10° away from the NGVS footprint; these images are of similar depth and image quality as the rest of the NGVS images and are thus useful for defining the characteristics of background contamination and assessing the variations in the Galactic foreground stellar population.

Calibration of the NGVS data is done through comparison to stars from the SDSS (York et al. 2000) through the MegaPipe calibration pipeline (Gwyn 2008), with rms errors of 0.01–0.02 mag. Unless noted otherwise, the resulting magnitudes are on the CFHT MegaPrime photometric system. Although the MegaPrime $u^*g'r'i'z'$ system shares similarities with the SDSS *ugriz* system, there are notable differences, especially with the u^* filter (e.g., Gwyn 2008; Ferrarese et al. 2012); any references to the SDSS *ugriz* system will be explicitly stated.

2.1. Photometry

Photometry of all objects on the final, stacked NGVS images was conducted using SExtractor (Bertin & Arnouts 1996); the details can be found in S. Gwyn et al. (in preparation). We use only the NGVS g' and i' photometry, as these were the first filters for which the entire NGVS footprint was completed. Future papers will make use of the $u^*i'K$ color–color diagram (Muñoz et al. 2014) for improved GC selection in the NGVS data set. Here we use the NGVS $g'i'$ photometry of sources based on an aperture diameter of eight pixels. The spatially dependent aperture corrections (due to small variations in the stellar point-spread function across the MegaCam field) were derived using samples of bright, unsaturated stars in each MegaCam field for each filter. The individual extinctions $A_{g'}$ and $A_{i'}$ values for each object were derived from the 100 μm dust maps from Schlegel et al. (1998). All magnitudes presented here have been corrected for these extinction values.

We have considered only those objects that lie outside regions masked by the reduction pipeline following the prescription of Gwyn (2008). Those are the regions around very bright, saturated stars that contain both saturated pixels, diffraction spikes, and elevated signal/noise in the immediate regions, rendering the photometry of objects located near such features suspect. While a survey such as the NGVS will contain many such bright stars, the small size of the individual masked regions ($\sim$0.01 arcmin^2 for the larger ones) will have an insignificant effect on the spatial number densities of objects over the large area being considered here; the total area around $\sim$200 masked regions around bright stars is $\sim$2.0 deg^2, or less than 2% of the total field area. For our study, we use only those objects in the NGVS catalog with $18.5 < g'_o < 24.0$; the bright cutoff is based on the saturation level of the brightest stars, and the faint g'_o cutoff is based on the approximate location of the GC luminosity function turnover for objects in the Virgo Cluster (Jordán et al. 2007; see also Section 3.4). This choice will maximize the number of GCs present in our analysis, while reducing the (increasing) contamination from unresolved background galaxies at fainter magnitudes.

Photometric incompleteness will not be a significant issue for this study. For much of the NGVS field area, image crowding is minimal and photometric incompleteness due to sky backgrounds will be insignificant. Our adopted faint-end cutoffs ($g'_o = 24$, $i'_o \sim 23.8$) are more than 1.3 mag brighter than the nominal S/N = 10 point source photometry for the entire survey ($g' \sim 25.9$ and $i' \sim 25.1$; Ferrarese et al. 2012), thus we expect our photometric completeness to be close to 100%. However, a pair of small regions within 2′ of the centers of M87 and M49 were not included in the SExtractor catalogs due to the high surface brightness background. For M87, a supplemental photometric catalog of sources in the central 4 deg^2 was derived from NGVS images with the light from M87 subtracted; any objects found and measured in the M87-subtracted images were folded in to the original catalog[21].

2.2. Point Source Selection

At the distance of the Virgo cluster, many (but not all) GCs are expected to be point sources in the NGVS i' images. At the faint photometric levels explored here, contamination by background galaxies can be significant, so the careful removal of clearly resolved objects is crucial in extracting the (comparatively) small number densities of GCs throughout the survey area. For a Virgo cluster distance of 16.5 Mpc, the median seeing of $\sim$0.″6 for most of the NGVS i' images corresponds to a physical size of 48 pc. Sources are expected to be marginally resolved for sizes of at least $\sim$0.1 FWHM (Harris 2009a), or $\sim$5 pc in our data. With typical Virgo cluster GCs having $r_h \sim$ 2–4 pc (e.g., Jordán et al. 2009; Strader et al. 2011; Puzia et al. 2014), we expect enough GCs to be marginally resolved such that we need to be mindful of throwing out significant numbers of bona-fide GCs through the use of strict point-source selection parameters.

Point sources were selected based on the concentration index $\Delta i' = i'_4 - i'_8$, the difference between the four-pixel and eight-pixel diameter i' *aperture-corrected* magnitudes. Only the i' magnitudes were used, as (1) the NGVS i' images were taken under the best seeing conditions and (2) the field-to-field variance in FWHM in the i' images was much less than that for the g' images. Thus non-stellar sources will be more clearly resolved in the i' images—tests using a similarly defined $\Delta g'$ index shows the $\Delta i'$ indication alone is an effective source discriminator.

As bright stars were used to create the aperture corrections described in the previous section, all true point sources should have $\Delta i' \sim 0$; resolved sources will have progressively larger (positive) values of $\Delta i'$. This is shown in Figure 1, which illustrates $\Delta i'$ values for sources in the entire NGVS catalog.

To determine the range of $\Delta i'$ appropriate for Virgo GCs, we have compiled a master catalog of confirmed GCs in some of the luminous Virgo cluster galaxies. This catalog includes all GCs

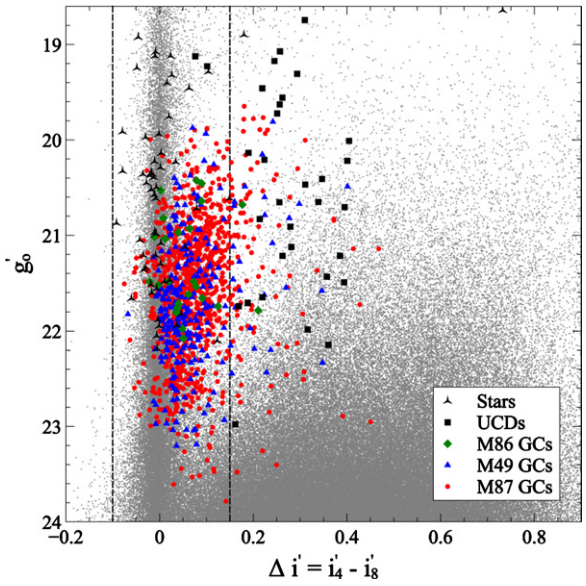

Figure 1. Plot of our i'-band concentration index $\Delta i' = i'_4 - i'_8$ vs. the total g' magnitudes for sources (only 5% of sources plotted for clarity) within the NGVS footprint (gray points); the stellar sequence at $\Delta i' \sim 0$ is clearly visible. Overplotted are NGVS-based photometry for 1216 GCs in 3 Virgo cluster galaxies that have spectroscopically derived velocities consistent with Virgo cluster membership (see the text for details). Also included are Virgo UCD galaxies from Brodie et al. (2011) and confirmed stars from Strader et al. (2011). Many of the confirmed GCs lie at larger $\Delta i'$ values than for stellar objects, indicating that a significant fraction of GCs are indeed marginally resolved on the $\sim$0.″6 seeing of our i' images. The dashed lines show the adopted $\Delta i'$ values for our point source catalog.

(A color version of this figure is available in the online journal.)

[21] A small number of objects near the center of M49 were missed in the SExtractor catalog, although a comparison of our source lists with confirmed M49 GCs show that a very small number (12) of the confirmed GCs were missed. The small number of missing objects will have no effect on the results presented in this paper, which are based on the larger-scale distribution of GCs throughout the Virgo cluster.

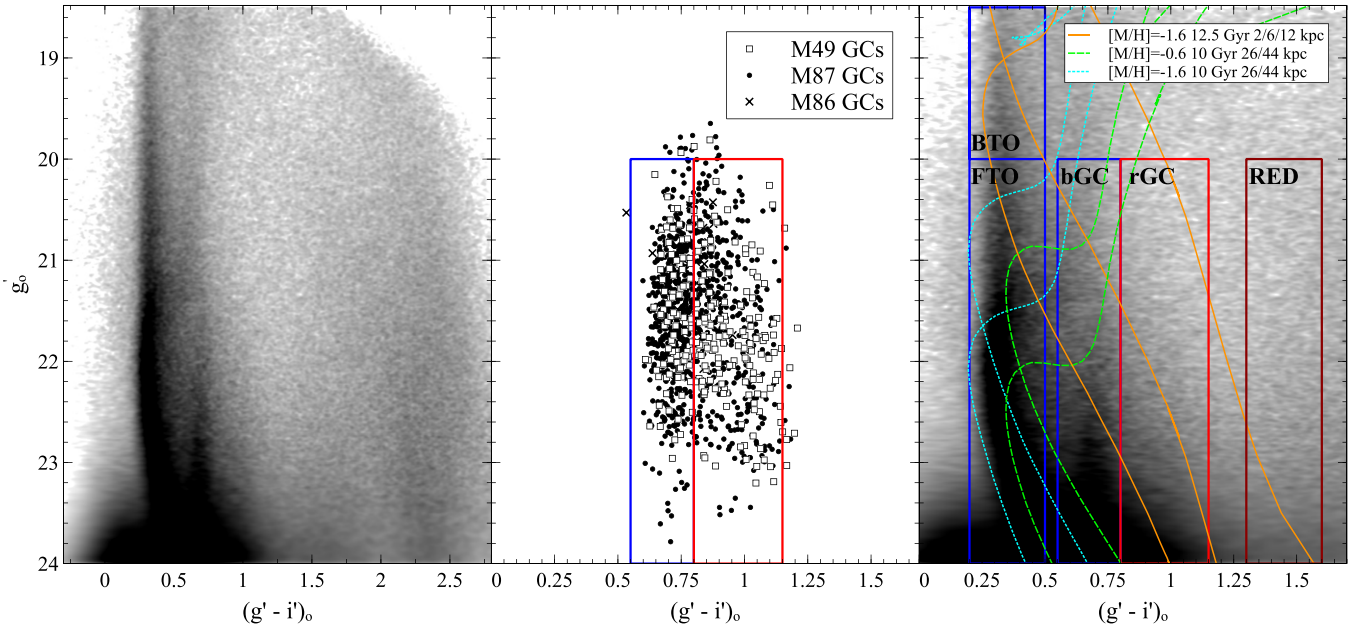

Figure 2. Left: g'_o, $(g'-i')_o$ Hess diagram for all point sources that satisfy the $\Delta i'$ criterion (Figure 1) and have $18.5 < g'_o < 24.0$. The colors and magnitudes for all sources have been smoothed by a value of the combined photometric errors and a constant value. Center: g'_o, $(g'-i')_o$ color–magnitude diagram for radial velocity-confirmed Virgo cluster GCs; the colored boundaries show the adopted color and magnitude criteria used for blue GCs (bGCs) and the red GCs (rGCs). Right: the g'_o, $(g'-i')_o$ Hess diagram for point sources overplotted with Marigo et al. (2008) isochrones with representative age/metallicity values appropriate for stars in the Milky Way (MW) halo at distances of 2–16 kpc (orange lines), and for stars expected to be in the Sagittarius dwarf galaxy (cyan and green lines) incorporating a spread in both the distance and metallicity; see the text for details. The boxed regions are the locations of the (from top left to bottom right) bright MW halo turnoff stars (BTO), faint [Sgr] turnoff stars (FTO), the blue globular cluster region (bGC), the adjoining red globular cluster region (rGC) and the red halo star populations (RED).

with spectroscopically derived velocities consistent with Virgo cluster membership, with M87 GCs from Hanes et al. (2001) and Strader et al. (2011),[22] M49 GCs from Côté et al. (2003), and M86 GCs from Park et al. (2012). We have also included 253 velocity-confirmed M87 GCs from E. Peng et al. (in preparation) that are neither in the Hanes et al. nor the Strader et al. catalogs. The final list includes a total of 1242 GCs from the 3 galaxies combined, of which 1218 have $g'i'$ photometry from the NGVS catalog (the very few missing objects are located either within masked regions or near the center of M49).

The $\Delta i'$ values for the spectroscopic GC sample are also plotted in Figure 1, along with 56 confirmed stellar sources in the M87 GC catalog of Strader et al. (2011), and 32 Virgo cluster UCDs from Brodie et al. (2011). Here we see that a significant number of Virgo GCs are marginally resolved, with $\Delta i'$ values systematically larger than that of the mean stellar sequence at $\Delta i' = 0$. A few GCs (and most of the cataloged UCDs) are well resolved in our data, with larger $\Delta i'$ values. As our goal is to extract as many GCs from the NGVS data without allowing many resolved contaminants into our sample, we have chosen our source selection criterion as those objects with $-0.10 < \Delta i' < +0.15$, based on visual inspection of Figure 1. This criterion contains 1094 confirmed GCs, or 90% of the complete sample. Hereafter, all objects that pass the $\Delta i'$ criterion will be referred to as point sources, although we re-iterate that some marginally resolved sources are included in this subsample. Our "point source" sample, $18.5 < g'_o < 24.0$ and $-0.10 < \Delta i' < 0.15$, for the entire NGVS region (excluding the four background fields) contains 792,790 objects.

[22] We consider all Strader et al. (2011) objects classified as GC or as transitional objects as bona-fide GCs.

2.3. Globular Cluster Color Selection

At the magnitudes and colors expected for Virgo cluster GCs, there will be a significant contribution from both foreground MW stars and from unresolved background galaxies. To select candidate GCs, we make use of specific regions within the g'_o, $(g'-i')_o$ CMD.

The left-hand panel of Figure 2 shows a smoothed Hess diagram for all of the objects in our point source catalog. Each object in the CMD has been Gaussian-smoothed by the photometric errors. The Hess diagram is comprised of many different populations, but is dominated by main-sequence turnoff (MSTO) stars with $(g'-i')_o \sim 0.4$ from both the intervening MW halo (and its substructures) and many nearby, low luminosity MW disk stars visible at $(g'-i')_o \sim 2.0$–2.5. At the faintest magnitudes there are many unresolved background galaxies at all colors. The locus of point sources at $(g'-i')_o \sim 0.6$–0.8 is the superposition of two distinct populations—those objects with $18.5 < g'_o < 21.0$ are largely red giant branch (RGB) stars from the Sagittarius dwarf galaxy (which passes through the center of the NGVS region; see Section 3.1.1), while fainter objects are GCs at the distance of the Virgo cluster.

To determine the appropriate $(g'-i')_o$ color range for Virgo GCs, the center panel of Figure 2 shows NGVS $g'i'$ photometry of the radial velocity-confirmed GC sample (see previous section). Most GCs have $0.55 < (g'-i')_o < 1.15$ and $g'_o > 20.0$, which we adopt as our color and magnitude criteria for GC selection over the entire NGVS data set. 1055 (or 87%) of the 1218 velocity-confirmed GCs in our sample satisfy all three criteria for selection as GCs.

As the range of $(g'-i')_o$ colors are indicative of the range of metallicities of the (assumed old) GCs, we have further divided our color criteria into a blue metal-poor GC population (bGC) and a red metal-rich GC population (rGC), with the dividing

color at $g'_o = 0.80$. This color corresponds to a metallicity [Fe/H]~ -1.05 based on the $(g-i)_o$–[Fe/H] relations from Lee et al. (2010) and Sinnott et al. (2010).[23] It is important to point out that this color choice was based not on a preferred metallicity, but on the most appropriate color above which very few Sgr stars will appear, aiding in our definition of the appropriate background (control) samples, described below.

2.4. Foreground/Background Contamination

The huge areal coverage of the NGVS and the use of a single broadband color to select GCs also means a large number of contaminating stars and galaxies is present.[24] The presence of numerous spatially distinct halo populations at different distances along the line of sight to the Virgo cluster makes the stellar contamination highly spatially dependent; such features include (but are not limited to) the leading arm of the Sagittarius dwarf galaxy (Belokurov et al. 2006), the Virgo Overdensity (VOD; Jurić et al. 2008), and the related Virgo Stellar Stream (VSS; Duffau et al. 2006). The structure of these features based on NGVS observations will be discussed in future papers in this series.

To illustrate this, the right-hand panel of Figure 2 shows isochrones approximating the expected stellar populations within the NGVS data. One of the leading arms of the Sagittarius dwarf galaxy ("Stream A" from Belokurov et al. 2006) passes through the NGVS field. Moreover, the mean heliocentric distance of this stream changes significantly over the NGVS region, from $d \sim 26$ kpc for our background B3 field to ~44 kpc in our background B4 field, with a range of 29–40 kpc for the NGVS science fields (Belokurov et al. 2006; Niederste-Ostholt et al. 2010). We have overplotted isochrones that span the ranges of both distance and metallicity of Sgr stars; we used the Bressan et al. (2012) isochrones of ages 10 Gyr, with metallicities of [M/H] ~ -1.6 and -0.6.[25] Most Sgr main-sequence and subgiant stars will have $g'_o > 20$ with colors $(g'-i')_o < 0.8$. Similarly, any MW halo main-sequence stars at $d < 20$ kpc appear at brighter magnitudes; these are indicated by the (old; 12.5 Gyr) Bressan et al. isochrones with [M/H] $= -1.6$, consistent with the mean metallicity of MW halo stars (Ryan & Norris 1991; An et al. 2013).

To quantify the spatially variable contamination from both halo sources and background galaxies, we have defined sections of the $g'_o, (g'-i')_o$ CMD (shown in Figure 2) to make the cleanest possible distinction between the many different populations present in the CMD.

1. BTO: $18.5 < g'_o < 20$, $0.2 < (g'-i')_o < 0.5$; largely contains "bright" turnoff stars from inner MW halo populations.
2. FTO: $20 < g'_o < 24$, $0.2 < (g'-i')_o < 0.5$; largely contains "faint" turnoff stars from both the Sgr dwarf and any MW halo stars at similar distances.
3. bGC: $20 < g'_o < 24$, $0.55 < (g'-i')_o < 0.80$; samples the Virgo blue GC population, as well as Sgr main-sequence, subgiant, and RGB stars, and inner halo main-sequence stars.
4. rGC: $20 < g'_o < 24$, $0.80 < (g'-i')_o < 1.15$; samples the Virgo red GC population, as well as inner halo main-sequence stars and faint MW disk stars.
5. RED: $20 < g'_o < 24$, $1.30 < (g'-i')_o < 1.50$; samples both inner halo main-sequence stars and any faint MW disk stars.[26]

From Figure 2, we see that much of the contamination for the blue GC (bGC) region of the CMD will come from Sgr main-sequence and subgiant stars, with contributions from closer halo stars (the faint turnoff (FTO) and bright turnoff (BTO) regions, respectively), while the primary contamination in the red GC (rGC) region is largely from halo stars and MW disk stars, with little contribution from the Sgr dwarf. Unresolved background galaxies contribute to all of the fainter regions.

To define the backgrounds for each of the bGC and rGC populations, we used a combination of regions both internal and external to the NGVS. These regions are shown in Figure 3, overlaid on a map of the point sources over the entire NGVS survey region (including the four background fields B1–B4). However, as the background fields sample parts of the MW halo that differ from that of the NGVS itself (indeed, one can see significant changes in stellar density in fields B1 and B2 versus B3 and B4), we have also defined 10 additional regions in the outskirts of the NGVS field (1) where no large galaxies are present and (2) far from the central regions of either of Virgo's two dominant subclusters.

For each of the regions illustrated in Figure 3, we have derived the surface number density Σ (in units of arcmin^{-2}) of point sources through star counts in the CMD regions defined above. We then compare the number densities of contaminating point source objects in the bGC and rGC regions with the densities of objects sampling the other regions of the CMD. These are plotted in Figure 4. The approximately linear behavior between the number densities of GC "contaminants" and that of the proxy regions of the CMDs shows our simple background models are reasonable. Furthermore, that the number densities of the control fields within the NGVS region are consistent (within the errors) with the four background fields indicate our choice of background fields was also reasonable. Put another way, the 10 intra-NGVS regions do not show any statistically significant excess of objects (over the four background fields) in the bGC and rGC regions that could be construed as a genuine GC population in the very outskirts of the Virgo cluster.

Figure 4 also includes the best-fit linear fits (using orthogonal weighted regression for points with errors in both axes; Feigelson & Babu 1992) to the number densities from all 14 control fields. The mean rms errors in the $\Sigma_{b,\mathrm{bGC}}$ relation is 0.013 arcmin^{-2}, and 0.011 arcmin^{-2} for the $\Sigma_{b,\mathrm{rGC}}$ relation. These values represent the minimum possible uncertainties in the estimate of the background populations, and lower limits on the number densities of GCs that could possibly be extracted from our data set.

3. ANALYSIS AND RESULTS

3.1. Number Density Maps

Due to the small number densities of GCs expected over such a wide area, and the significant number of "background" objects, it is necessary to create smoothed two-dimensional (2D) surface

[23] We first converted our MegaCam $(g'-i')_o$ color to the SDSS $(g-i)_o$ color using the relations in Gwyn (2008).

[24] Use of multiple colors will reduce the background contamination (e.g., Rhode & Zepf 2004; Tamura et al. 2006a; Kim et al. 2013); future studies will make use of the multi-color NGVS data (e.g., Muñoz et al. 2014).

[25] Our results do not, however, depend strongly on the representative values used here.

[26] We avoid the red M dwarf sequence at $(g'-i')_o > 2$, which will have little predictive power as control samples for the GC populations we are considering here.

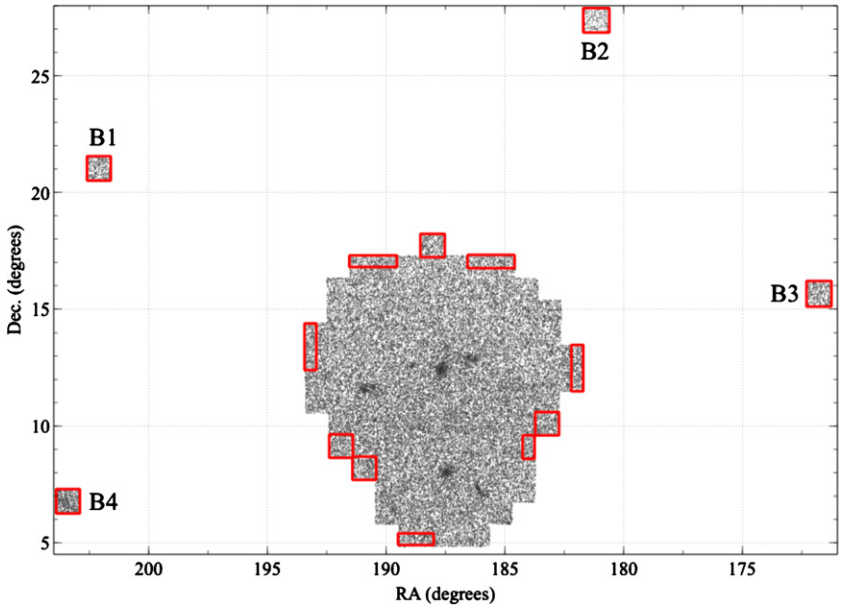

Figure 3. Spatial distribution of point sources with $18.5 < g'_o < 24.0$ within the NGVS survey area (center) and the background fields B1–B4. Dense regions around the major Virgo galaxies are apparent; however, a large fraction of the points far from the galaxies are either foreground Milky Way stars or are unresolved background galaxies. The boxes (red in the online version) indicate the locations of the background regions used for estimation of background contamination in our point source catalog.

(A color version of this figure is available in the online journal.)

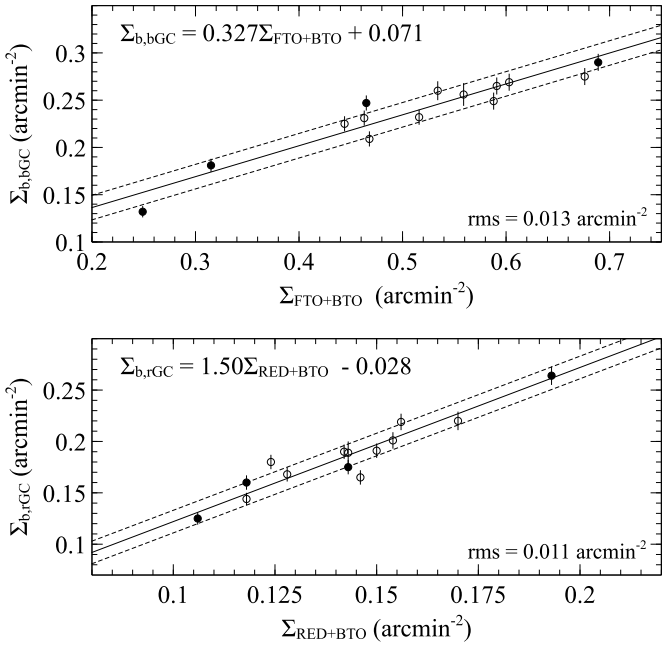

Figure 4. Measured stellar surface densities (in arcmin^{-2}) for the expected backgrounds for each of the blue and red GC populations based on raw number counts in the four control fields (filled circles) and that of 10 regions on the outskirts of the NGVS field (open circles). Top: the surface density of objects with colors of blue GCs as a function of the combined number density of Sgr turnoff stars (FTO) and halo turnoff stars (BTO). Bottom the surface density of objects with colors and magnitudes consistent with red GCs as a function of the combined number density of halo turnoff stars (BTO) and halo/disk stars (RED). In both panels, the best fitting line (and uncertainty) is shown.

density maps of the various stellar/extragalactic/GC populations present in our data.

All spatial maps presented here were created by replacing the position (α, δ) of each point source from the different regions of the CMD in Figure 2 with a circular Gaussian kernel with either a constant or variable FWHM (see below). The results were mapped onto a full mosaic image of the NGVS field of view with a pixel scale of $\Delta\alpha = \Delta\delta = 0.''238$. To account for the small variations in the true area coverage of each pixel over the large field of the NGVS, a pixel-area map was constructed in order to convert the image from units of pixel^{-2} to units of arcmin^{-2}. We stress that all maps presented here are based on the *observed* number densities of point sources with $g'_o < 24$; unless explicitly stated, conversion of our Σ_{GC} values to a total GC number density $\Sigma_{GC,tot}$ requires a correction factor of 2.05 ± 0.22. This factor is based on the detection of the top 56% ± 6% of the GCLF (see Section 3.4), with an additional correction for the 13% of GCs that are removed by the point source classification described above.

While such smoothing of the data will cause some information to be extended outside the NGVS boundary, such losses are small and will not significantly affect our presented results. Similarly, the number of sources removed in masked regions of the NGVS will also not affect our results in any meaningful way.

3.1.1. Adaptive Smoothing

Due to the large dynamic range of observed number densities Σ_{GC} expected in our data, from the many GCs near the M87 core to any sparse IGC population, we first applied an adaptive-smoothing approach to the data. We created four point source lists based on the various regions of the CMD shown in Figure 2: the bGC region, the rGC region, the combined BFTO and FTO regions (background for the bGC population), and the combined BTO and RED regions (background for the rGC population). The position of each source was replaced by a circular Gaussian with $\sigma = 3.5r_n$ (Gaussian FWHM $= 8.26r_n$), where r_n is the radial distance from each point to its nth nearest neighbor. To avoid any possible artifacts that might result from the addition/subtraction of images with very different smoothing values, the value of n for each list was chosen such that the peak of

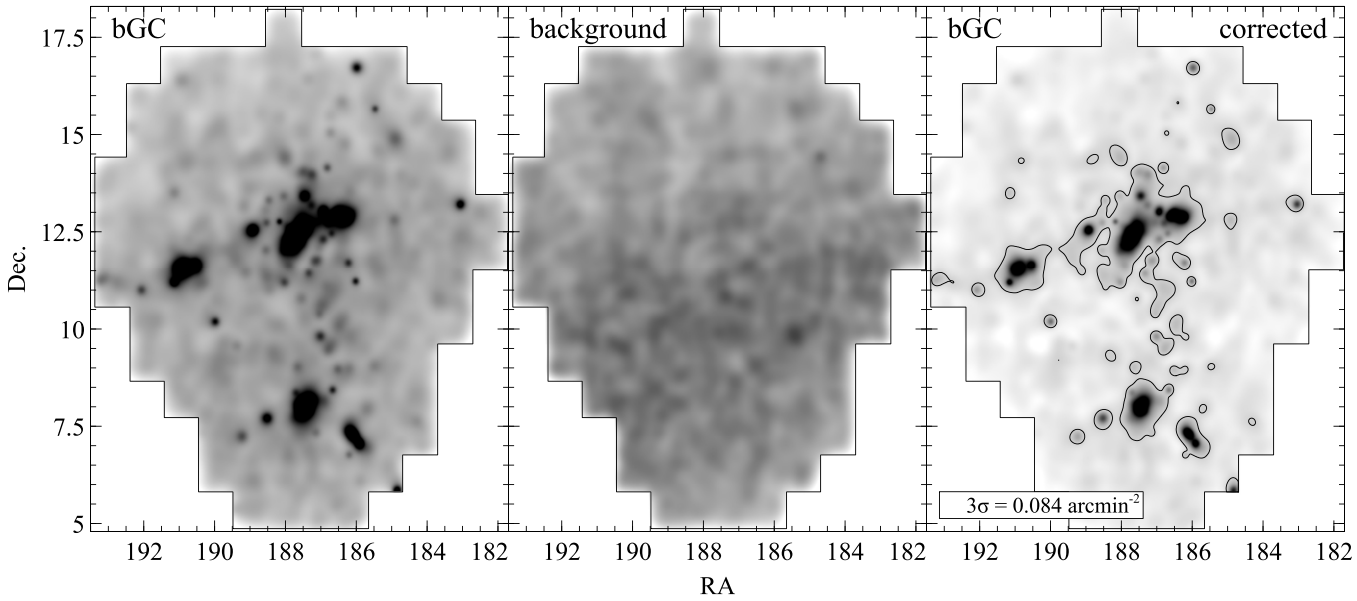

Figure 5. Adaptive-smoothed bGC surface density maps. Left: "raw" smoothed map for point sources with colors and magnitudes consistent with being blue globular clusters (bGCs) in the Virgo cluster. Center: model map for the expected bGC background, constructed through a (scaled) smoothed map of the combined BTO and FTO point sources. The leading arm of the Sgr dwarf can be seen as a positive enhancement through the center of the NGVS region. (Note: grayscale stretch in this image different from left-hand image in order to enhance density variations). Right: background-subtracted map showing the surface density map of blue GCs in the Virgo cluster. The single contour indicates the 3σ level.

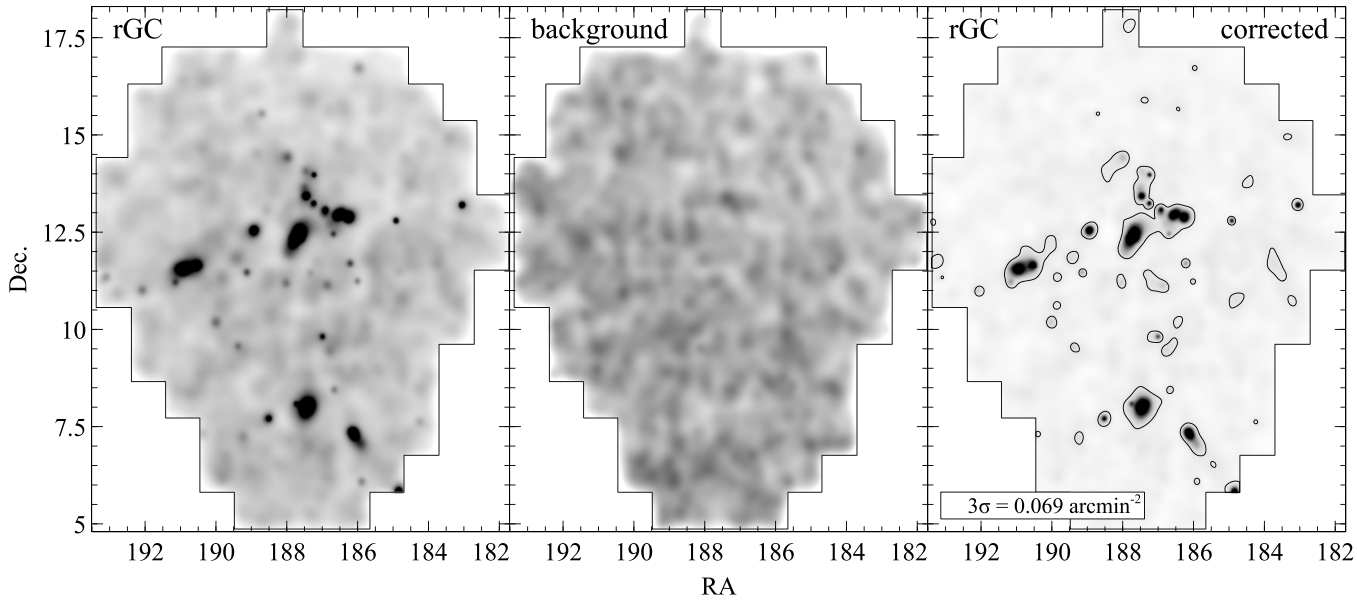

Figure 6. Similar to Figure 5, but showing the adaptive-smoothed rGC surface density maps. Left: "raw" map point sources with colors and magnitudes consistent with being red globular clusters (rGCs) in the Virgo cluster. Center: model map for the expected rGC background, constructed through a (scaled) smoothed map of the combined BTO and RED point sources. (Note that the grayscale stretch in this image is different from left-hand image in order to enhance density variations.) Right: background-subtracted map showing the surface density map of red GCs in the Virgo cluster. The single contour indicates the 3σ level.

the r_n distribution for the lowest density regions were matched at a value $r_n \sim 0.^{\circ}065$ (FWHM $= 32'$), which approximates the largest smoothing value used in the next section. We have adopted the following for each of the four maps: bGC:r_{14}, rGC:r_{10}, BTO+FTO:r_{26}, and BTO+RED:r_8.

The resulting adaptive-smoothed maps for each of the bGC and rGC populations are shown in Figures 5 and 6, respectively. The left-hand panels of both figures show the smoothed map for all point sources with colors and magnitudes lying in the bGC/rGC regions of the CMD—the concentrations of sources around the many large galaxies in Virgo are readily visible. The center panel of both figures shows the predicted background map created through the appropriate map (BTO+FTO and BTO+RED, respectively, for the bGC and rGC maps) and applying the $\Sigma_{b,\mathrm{bGC}}$ and $\Sigma_{b,\mathrm{rGC}}$ relations from Figure 4. Both background maps show spatial variations, showing that adoption of a constant background value is insufficient.

The bGC background map in Figure 5 merits special mention, as the smoothed BTO+FTO map (largely a map of MSTO stars in the MW halo) shows a distinct positive density enhancement from $\alpha \sim 183^{\circ}, \delta \sim +11^{\circ}$, through the center of the NGVS field, to $\alpha \sim 191^{\circ}, \delta \sim +8^{\circ}$. This feature is Stream A of the leading arm of the Sgr dwarf galaxy. While a full discussion of this and other MW features in the NGVS data are left for future papers in

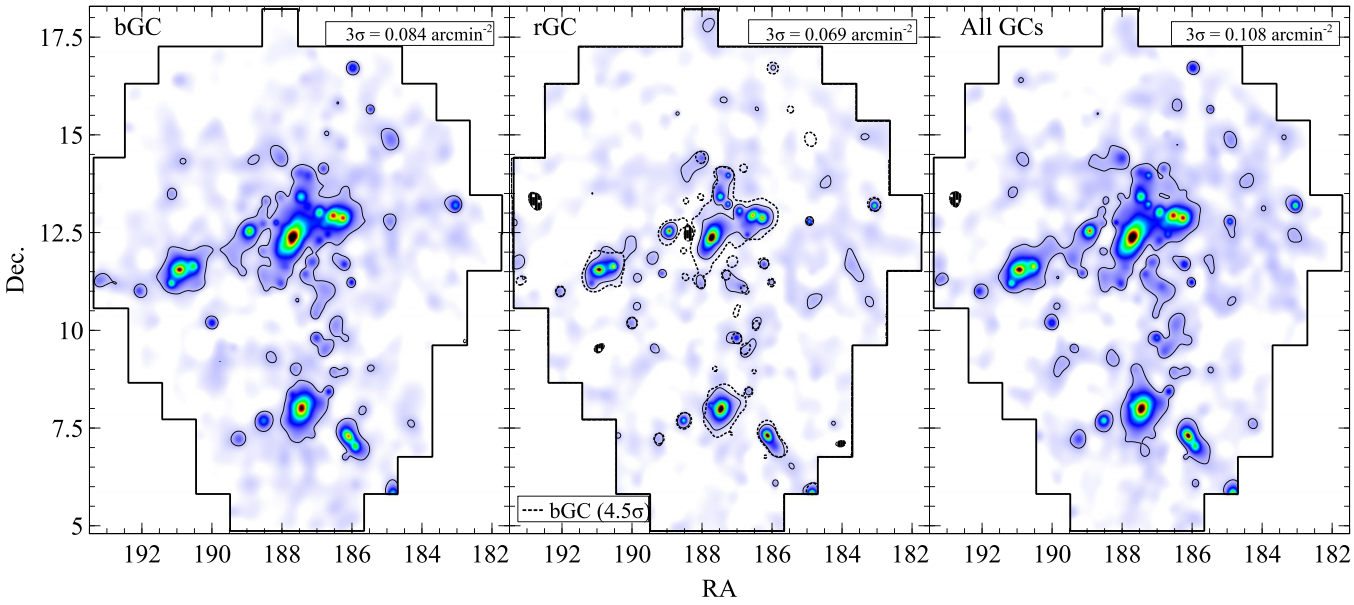

Figure 7. Adaptive-smoothed surface density maps of the GC populations in the Virgo cluster (left) blue GCs, (center) red GCs, and (right) all GCs. In each map, the 3σ contours are shown as solid lines. Hatched regions denote the -3σ contours in the center and right panels. For the center panel, the dashed line represents the surface density map of the bGC population at the same density fraction as shown for the rGC population; see the text for details.

(A color version of this figure is available in the online journal.)

this series, it is clear that the entire width of this stream appears in our data. While density variations in the rGC background map in Figure 6 are less apparent, there is a slight increase in the number density of stellar objects toward lower δ. This is due to the presence of the VOD, which covers over $\sim$2000 deg^2 and whose stars have distances of $d = 6$–20 kpc (see Bonaca et al. 2012, and references therein). The spatial peak of the VOD is located outside the NGVS region toward the South; this feature is the dominant background for the (shallower) study of Virgo's GC populations by Lee et al. (2010).

The right-hand panels in Figures 5 and 6 shows the resulting background-subtracted number density maps of the blue GC and red GC populations in the Virgo cluster. The single contour in these plots is the 3σ level; the background noise σ for these maps (and others) was estimated through computing the standard deviation of the surface densities within six 300 $\times$ 300 pixel ($\sim 71' \times 71'$) regions in the outer regions of the map (far from any obvious excesses). These regions are large enough that we are sampling true variations in σ for all smoothing values applied. The noise in each map is the combination of the median σ for the six regions and the background rms errors.

The background-subtracted rGC and bGC maps are markedly different from each other. We illustrate this in Figure 7, which shows the final, background-corrected bGC and rGC maps as well as the combined GC map (the sum of the bGC and rGC maps). Virgo's blue GC population appears to be more spatially extended than the red GC population (at the 3σ background level). A more extended blue GC distribution is also found for GC systems belonging to individual galaxies (e.g., Geisler et al. 1996; Lee et al. 1998; Bassino et al. 2006; Harris 2009b; Kartha et al. 2014) and in the Virgo cluster from Lee et al. (2010).

However, it is possible that the spatial differences could be due to the fact that the contour levels shown in the figures are drawn at σ levels that are relative to the background rather than to the density level of the GC population itself. To foster a more direct comparison between the two populations, in Figure 7, we plot bCG contours drawn at the same density level as the rGC contours. The 3σ level in our rGC map corresponds to a level 2.3$\times$ larger than the mean observed rGC density over the entire NGVS. The same fractional level in the bGC map lies at an observed $\Sigma_{\rm bGC} = 0.128$ arcmin^{-2}, or 4.5σ. This comparison shows that the bGC population is still more extended than that of the rGC population around the larger galaxies/subclumps in Virgo, but is particularly evident in the Virgo A = M87 region. This is the clearest demonstration to date that the difference in concentration between the red and blue GC populations is generic to all GC systems in all galaxies, being readily apparent over the entire Virgo cluster. We defer further discussion of specific features on these maps to Section 3.2.

As a test of our derived background σ values for each map in Figure 7, we also plotted the -3σ contours as hatched regions. There are three areas of the rGC map that show 3σ "holes," including a feature 0.°7 east of M87. All of these regions, however, are areas where (1) the surface densities of objects in the rGC region of the CMD show depressed values and (2) where there is an observed enhancement in the background. The negative feature near the eastern edge of the NGVS field at $\alpha \sim 192.°8$, $\delta \sim +13.°3$ coincides with the location of the galaxy cluster A1627, but it is unclear if this is the reason for the enhanced background. The locations of 15 other galaxy clusters in the Abell et al. (1989) catalog that lie within the NGVS do not correspond to *any* features, positive or negative, in either of the background maps. That such "holes" exist on our map does indicate that the $\sigma_{\rm rGC}$ value may be a slight underestimate. For consistency, we continue to use the derived $\sigma_{\rm bGC}$ and $\sigma_{\rm rGC}$ values and urge the usual caution when interpreting 3σ features. Similar caution is urged near the NGVS boundary in the maps, where artifacts can be introduced from the smoothing of objects outside (but not inside) the NGVS boundary.

3.1.2. Constant Smoothing

For comparison purposes, we have also created smoothed GC number density maps using circular Gaussian kernels with a fixed FWHM = $10'$ and FWHM = $30'$, corresponding to

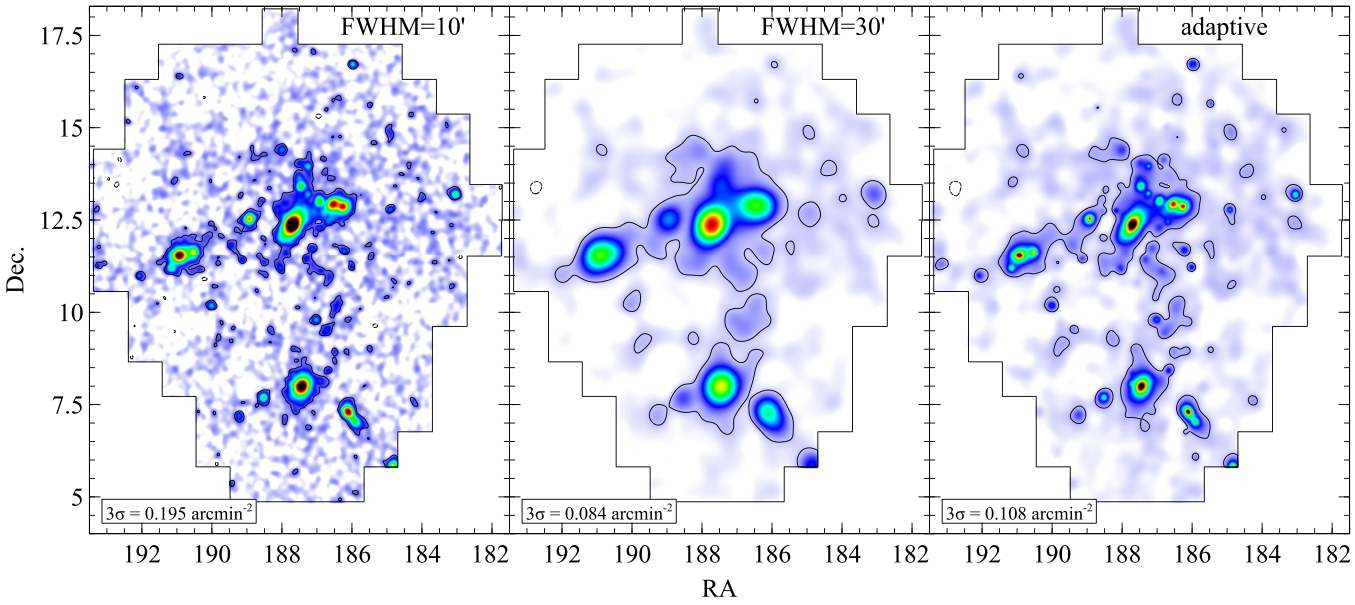

Figure 8. Surface density maps of the observed GC (bGC+rGC) populations in the Virgo cluster (left) map smoothed with a Gaussian kernel with FWHM = 10′ (center) GC map smoothed with a Gaussian kernel with FWHM = 30′ (right) GC map smoothed with a varying (adaptive) FWHM. In each map the 3σ contours are shown as solid lines. Dashed lines show the −3σ contours.

(A color version of this figure is available in the online journal.)

physical scales of 48 kpc and 144 kpc, respectively. These maps were created (and the noise σ derived) in the same way as the adaptive-smoothed maps. The FWHM = 10′ map (left-hand panel of Figure 8) puts emphasis on any smaller-scale structures in the GC maps, at the expense of a higher background noise. The center panel of Figure 8 shows the more heavily smoothed FWHM = 30′ map, which is useful for probing the much lower GC number densities in the regions between the galaxies. Furthermore, as the FWHM = 30′ map is similar in resolution (and background noise level) of the Lee et al. (2010) map of Virgo's GC population, this map will be used to foster a useful comparison with that work.

All three maps show (at different levels of depth and resolution) the cluster-wide distribution of GCs in the Virgo cluster, which shows a wealth of substructure from the large GC populations around the luminous Virgo galaxies to the sparse outer regions. The adaptive-smoothed map will be used for much of the following analyses, as it shows both fine resolution in the cores of large galaxies (with smoothing values FWHM ∼ 3′–5′), to much larger smoothing values (typical FWHM ∼ 20′–40′) in the less dense regions of the NGVS. The constant smoothed maps will be used to test the validity of features detected in, and the number density profiles Σ_{GC} derived from, the adaptive-smoothed maps. We stress that all of the features indicated in the following sections are not artifacts of the adaptive-smoothing process—the same features are also visible in at least one of the constant FWHM maps.

3.2. The Spatial Distribution of Virgo's GC Populations

Figure 9 shows the final, adaptive-smoothed map of Virgo's GC (bGC+rGC) population, overlaid with the locations of the 1467 Virgo cluster member galaxies from the VCC that lie within the NGVS footprint. As expected, the majority of GC features above $\Sigma_{GC} = 0.108$ arcmin$^{-2} = 3\sigma$ are spatially co-incident with Virgo galaxies. In particular, the largest/densest concentrations of GCs are located in the regions surrounding the four largest substructures of the Virgo cluster:

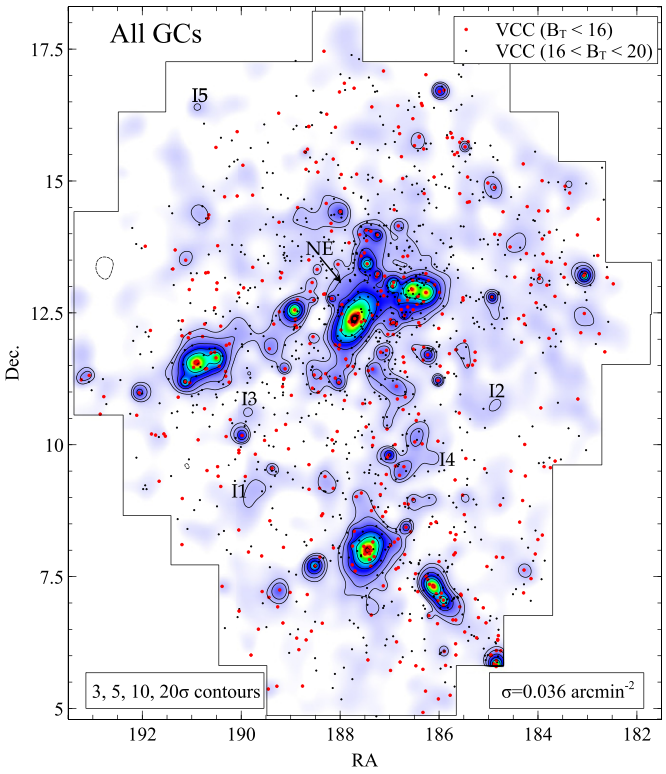

Figure 9. Adaptive smoothed GC number density map of the Virgo Cluster with the noted contours of the observed number densities Σ_{GC}. The filled circles (red in the online version) denote the positions of Virgo member galaxies from the VCC (Binggeli et al. 1985) that lie within the NGVS boundary and have B_T < 16; the black dots represent VCC galaxies with 16 < B_T < 20. I1–I5 denote map features where no VCC galaxies are present and "NE" refers to a possible excess of GCs near M87; see the text for details.

(A color version of this figure is available in the online journal.)

Virgo subcluster A (centered on M87), subcluster B (centered on M49), subcluster C (centered on M60, center left), and the (infalling?) subcluster centered on M86 to the right of M87.

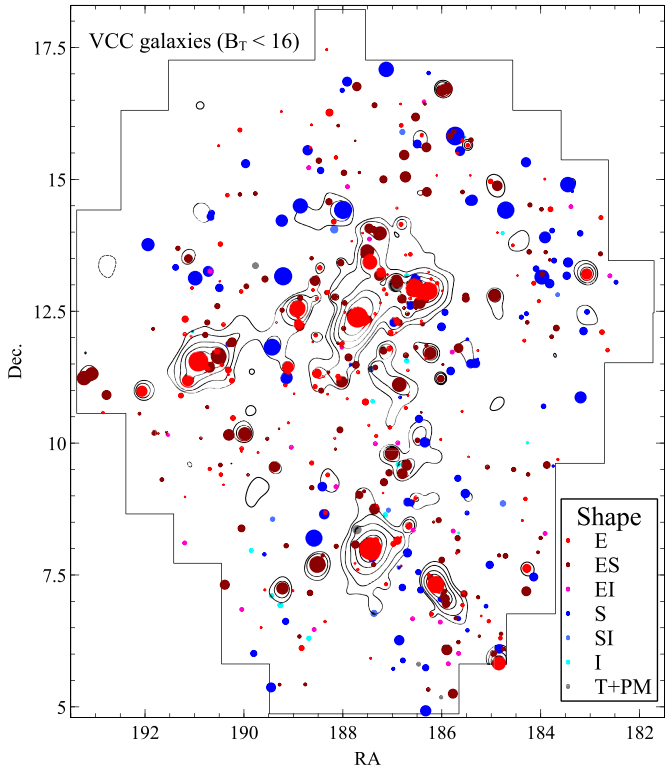

Figure 10. Adaptive smoothed GC number density map; the contours are the same as in Figure 9. The filled circles show the locations of those VCC galaxies within the NGVS with $B_T < 16$; the circle sizes are inversely weighted to B_T. The galaxies are color-coded based on a new classification system using the shapes of the galaxies in deep NGVS images; see the text for more details. E = elliptical, ES = elliptical–spiral (transition), EI = elliptical–irregular (transition), S = spiral, SI = spiral–irregular (transition), I = irregular, T+PM = tidal and/or post merger.

The figure also indicates the locations of the brighter Virgo galaxies ($B_T < 16$). What may seem surprising is the large number of bright VCC galaxies that do *not* have GC peaks in the map. Due to the (necessarily) large smoothing values applied, any GC systems with small GC populations (many dwarf galaxies), or low density GC systems (e.g., many late-type galaxies) will be smoothed below the 3σ contour. Although the GC systems of many spirals are smoothed to below the 3σ level in the number density maps, their numbers are included when computing the total number of GCs in the Virgo cluster in Section 3.4.

Figure 10 shows the location of all VCC galaxies, brighter than $B = 16$, that are confirmed or probable cluster members located inside the NGVS footprint. To provide a first glimpse into the connection between the GC distribution and galaxy morphology, galaxies have been divided into seven broad categories based on their appearance (i.e., isophotal structure) at optical (NGVS) wavelengths. Full details on this scheme, including classifications for all Virgo galaxies within the NGVS, will be presented in a future paper in this series. Briefly, the seven categories—E, ES, EI, S, SI, I, and T+PM—refer to the global structure of the galaxy; i.e., E galaxies have smooth and regular isophotes that are nearly elliptical in shape, S galaxies show unambiguous spiral arm patterns, and I galaxies have a more irregular appearance. The ES, EI, and SI categories include (transitional) galaxies that cannot be assigned uniquely to the E, S, or I categories (i.e., nearly elliptical galaxies with irregular, large-scale star formation superimposed would be classified as type EI). The seventh category, T+PM, refers to galaxies that are experiencing strong tidal distortion or show evidence for post-merger evolution.

3.2.1. GCs in Virgo Galaxies

The observed distribution of Virgo cluster GCs shown in Figures 9 and 10 largely mirrors that of the distribution of the luminous early-type (E and ES) galaxies, although the spiral galaxy M88 (above center) is a strong counter-example. This is merely the consequence of early-type galaxies tending to have more GCs per unit luminosity (the specific frequency S_N) than do most spirals (e.g., Harris 1991).

The bulk of the GCs are located in the Virgo A region surrounding M87, the dynamical center of the Virgo cluster. Not only are many of the GCs around M87 distributed along the galaxy major axis (e.g., McLaughlin et al. 1994; Côté et al. 2001; Strader et al. 2011; Forte et al. 2012), but the GC distribution of the entire region appears asymmetric, where more material is seen to extend to larger distances beyond M87's NW major axis versus the SE major axis. While some of the irregular distribution is due to GCs in the other bright galaxies in the region, we also see evidence of additional GC populations that will be discussed in Section 3.3.2.

The Virgo A region around M87 shows many spatial substructures in the diffuse light (Mihos et al. 2005); our GC maps indicate this is also true for the GCs. Such substructure is not only due to the presence of the many luminous galaxies within Virgo A, but also smaller, less luminous features that are the result of a continuing and complex evolutionary history (e.g., Mihos et al. 2005; Janowiecki et al. 2010; Romanowsky et al. 2012; Zhu et al. 2014). In Figure 11, we superpose our GC contour map over the ultra-deep *V*-band images of Virgo from Mihos et al. (2005) and Janowiecki et al. (2010), which show the distribution of diffuse light as faint as $\mu_V \sim 28$ mag arcsec^{-2}. The GC contours and the diffuse light surrounding M87 and M49 are very similar, down to levels $\mu_V \sim 27$ mag arcsec^{-2}. Such comparisons are difficult at fainter levels due the larger uncertainties in both the GC number densities and the diffuse light. The smoothing of our maps does not allow for detection of the many *fine* structures and stellar streams visible in Figure 11 (and described in Mihos et al. 2005; Janowiecki et al. 2010). The total luminosities of such streams in both the M87 and M49 regions are very low (typically $\sim 10^8\ L_\odot$) and would at most contain a handful of GCs, although directed spectroscopic studies might prove interesting.

Also present in the deep *V*-band images are features due not to Virgo Cluster ICL, but to galactic cirrus (see Mihos et al. 2005; Davies et al. 2012, for more details). Comparison with these features (arrowed in Figure 11) with the GC maps show that none are related to enhancements in the GC maps. Indeed, the magnitudes in our point source catalog have already been extinction corrected according to the Schlegel et al. (1998) dust maps based on *IRAS* 100 μm maps, which also show these brighter cirrus features.

3.2.2. Isolated GCs?

While most of the GCs shown in Figures 9 and 10 are coincident with known Virgo galaxies, there are a number of regions with no known cluster galaxies that lie at greater than 3σ above the background in the summed bGC + rGC map that could represent regions of Virgo with a "pure" population of IGCs. These features are labeled I1–I5 in Figure 9. One such feature (I5) is the GC system of NGC 4651, which is not within the VCC survey area. The remaining four features,

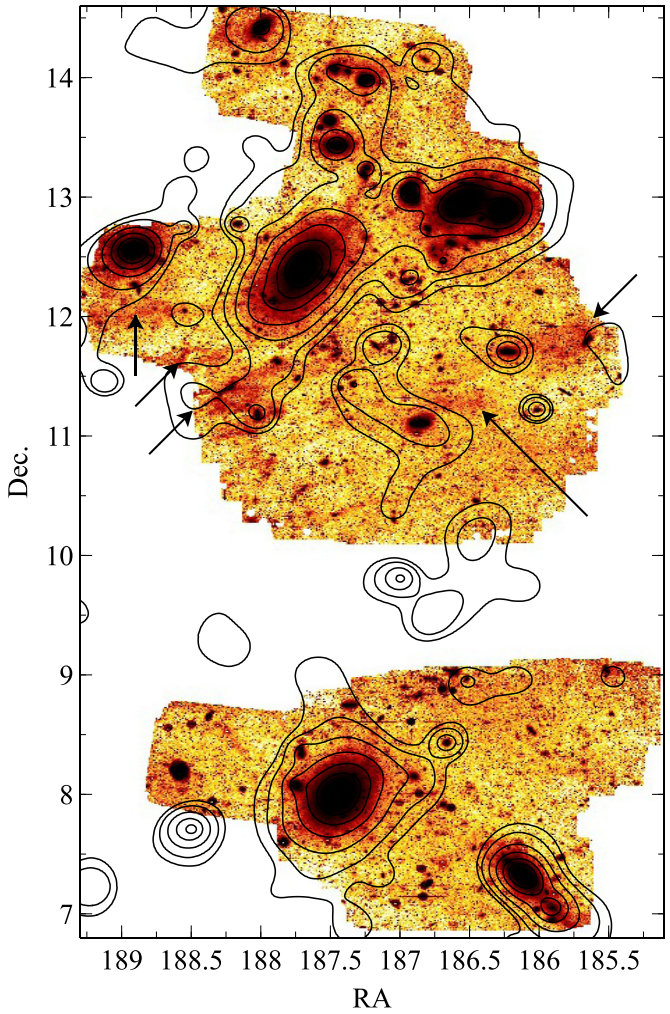

Figure 11. Adaptive-smoothed GC map ($3\sigma, 5\sigma, 10\sigma, 20\sigma, 40\sigma, 80\sigma$ contours) plotted on the deep *V*-band mosaic image from Mihos et al. (2005) and J. C. Mihos et al. (in preparation), where the lowest level grayscale represents $\mu_V \sim 28.0$ mag arcsec^{-1}. Note that many of the low surface brightness features below M87 are galactic cirrus (marked by arrows) and not Virgo Cluster ICL.

(A color version of this figure is available in the online journal.)

however, lie between 3σ and 4σ above the background. As our background maps are based solely on the spatial distributions of two rather different populations, foreground MW halo stars and background galaxies, variations in the number densities of either of these populations (e.g., background galaxy clusters) could lead to a *small* number of spurious 3σ detections. We do find one region in the total GC map in Figure 9 that lies $>3\sigma$ *below* the background, so it is possible that many (if not all) of these four isolated features are spurious. Analyses in future papers where the background contamination will be reduced through the additional use of u^*- and *K*-band imaging (e.g., Muñoz et al. 2014) and/or spectroscopic followup will be required to provide any further insight on these features.

3.3. The Extended GC Populations of Virgo A (M87) and Virgo B (M49)

Due to the smoothing applied to create the GC surface density maps, a detailed look of the spatial distribution of GCs around individual Virgo cluster galaxies is beyond the scope of this paper, and are left for future papers in the series where either multiple colors are used to reduce the background noise and/or spectroscopic confirmation of cluster membership of individual GCs is done. However, it is illustrative to use our maps to look at the extent of the GC systems around the two most massive subclusters in Virgo, shown in Figure 12. The sheer complexity of the distribution of GCs in the Virgo A region is presumably a combination of GCs from M87, surrounding galaxies (including M84 and M86 to the NW), and any possible extended IGC population. The Virgo B region is also surrounded by the GC systems of many (smaller) galaxies. We can characterize the outer regions of the GC system of each galaxy through fitting ellipses to the smoothed maps.

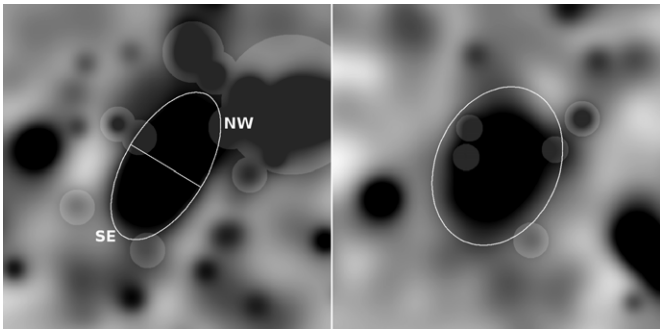

Figure 12. Grayscale images of the central $3^\circ \times 3^\circ$ region of the adaptive smoothed GC number density maps of M87 (left) and M49 (right). The masked regions for the ellipse fitting are shown, as are ellipses with $r_{\rm maj} = 45'$ (with $\epsilon = 0.5$ for M87 and $\epsilon = 0.25$ for M49) that represent the galactocentric distance at which the rGC population is consistent with zero; see the text for details.

3.3.1. Elliptical Profiles

For the ellipse fitting, we use the maps with the variable FWHM as they (1) allow for small smoothing values in regions with high $\Sigma_{\rm GC}$ (e.g., the cores of M49 and M87), and (2) have a relatively low noise $\sigma_{\rm GC}$ to allow us to define the presence (if any) of any extended GC component around these galaxies. The use of a spatially variable FWHM, however, comes with caveats of its own, as the smoothing in the outer regions of M87 and M49 can be FWHM $\sim$ 30–40′ and can have an adverse affect on some of the measured parameters. Where possible we make use of the constant FWHM maps (see Figure 8) to assess our results.

By fitting ellipses to both GC systems, we are making the assumption that any GCs within the ellipses are (nominally) associated with each galaxy, and any objects that deviate strongly from such a regular system would be considered non-members. Without spectroscopic confirmation of individual GC candidates, however, such a simplistic assumption is necessary. Due to spatial irregularities in the low density outer regions of each subcluster, we place strong constraints during the ellipse fitting process. We used circular masks to remove as many GCs from neighboring galaxies as possible. The masked regions are shown in Figure 12.

We used the ELLIPSE task in IRAF, where an iterative approach to modeling the elliptical isopleths is carried out for major axis radii from $r_{\rm maj} = 1$ pixel (0.″2) to 350 pixels (83′) for both galaxies on the rGC, bGC, and GC adaptive-smoothed maps from Figure 7. The fits continued until the number of rejected pixels exceeded 50% of each ellipse. The centers of the ellipses were fixed to the centers of each galaxy. We also fixed the position angle of the M87 GC system at PA $= 149^\circ \pm 4^\circ$, as tests showed the major axis of M87's GC system to be relatively constant with radius. This value is consistent with that of M87's

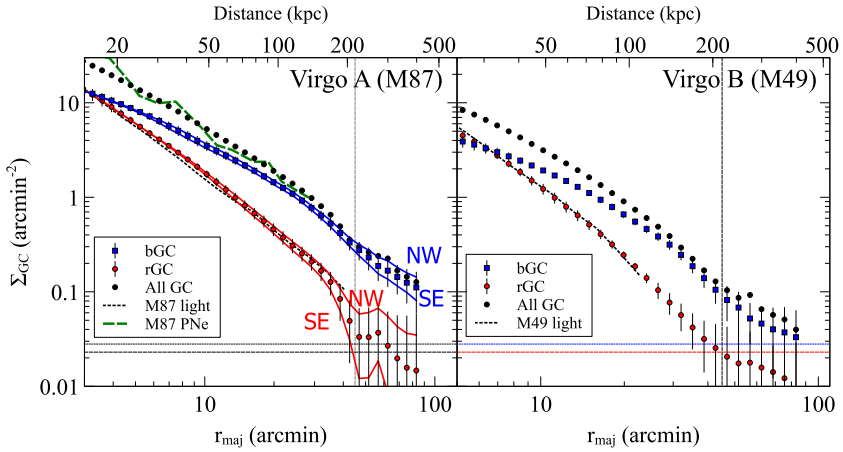

Figure 13. Surface density profiles for the globular cluster populations around M87 and M49 based on ellipse fitting to the adaptive-smoothed GC maps. Shown are the profiles for the red GC population (circles; red in the online version), the blue GC population (squares; blue in the online version) and the summed GC (bGC+rGC) population (black circles). The black dashed lines denote the *V*-band light profiles from Janowiecki et al. (2010), arbitrarily scaled vertically to match the red GC population. The thick dashed line (green in the online version) denotes the spatial densities Σ_{PN} of M87's planetary nebulae (PNe) from Longobardi et al. (2013), scaled up by a factor of 5.5 to compare directly with the summed GC profile. The solid lines denote the profiles resulting from ellipse fitting the NW and SE regions of M87. The horizontal dashed lines illustrate the 1σ level based on the uncertainties in the background for the rGC and bGC populations, respectively. The vertical dashed line denotes the radius $r_{maj} = 45'$ outside which the red GC population disappears. Note that only those parts of the profiles outside $r_{maj} \sim$ FWHM for the smallest smoothing values are shown: $r_{maj} > 3'$ (M87) and $r_{maj} > 5'$ (M49).

(A color version of this figure is available in the online journal.)

light profile (Janowiecki et al. 2010). For M49, we allowed the ellipticity ϵ to vary and fixed the PA $= 156^\circ \pm 3^\circ$; again, this PA range for the GC system mirrors that of the underlying light (e.g., Janowiecki et al. 2010).

The derived ellipticities ϵ for the isopleths are strongly affected by smoothing with a circular kernel. To determine outside what radii such effects are minimized, we performed ellipse fits to the FWHM $= 10'$ map, where such effects should be minimal for $r \gtrsim 3\times$FWHM $= 30'$ (e.g., Schweizer 1979). We cannot provide a reliable ellipticity profile of the GC systems interior to this. We found that ϵ derived from both the adaptive-smoothed and constant smoothed maps for $30' < r_{maj} < 50'$ to be similar : $\epsilon_{M87,GC} = 0.50 \pm 0.05$ and $\epsilon_{M49,GC} = 0.25 \pm 0.05$. We adopt these values for defining the GC systems in the outermost regions (see Figure 12). The M87 value can be compared to previous studies that show $\epsilon_{M87,GC}$ increases with radius (McLaughlin et al. 1994; Strader et al. 2011; Forte et al. 2012), and our results suggest this trend continues to larger radii. The resulting number density profiles Σ_{bGC}, Σ_{rGC}, and Σ_{GC} are shown in Figure 13. The uncertainties are based solely on the rms errors of the intensity around each ellipse. The adopted errors are large as the data points are not completely independent of each other as each ellipse fit is based on the results of the previous ellipse; see Jedrzejewski (1987) and Busko (1996) for technical details of the ellipse fitting algorithm and associated uncertainties. However, the size of the error bars gives a reasonable view of the uncertainty at any one point, particularly in the outermost regions where the uncertainties due to the background are significant. Only data points outside $r_{maj} = 3'$ for M87 and $r_{maj} = 5'$ for M49 (corresponding to the smallest smoothing FWHM in the core region of each galaxy) are shown as all surface densities interior to this are smoothed down. The GC systems at smaller radii around both galaxies have been previously studied in greater detail (McLaughlin et al. 1994; Harris et al. 1998; Kundu et al. 1999; Lee & Kim 2000; Tamura et al. 2006b; Waters et al. 2009; Harris 2009b; Forte et al. 2012). For comparison, M87's *V*-band light profile (from the Schmidt images of J. C. Mihos et al., in preparation) has also been included. Previous studies have shown that the surface density profiles of the red GC systems in elliptical galaxies closely follows that of the underlying light (e.g., Geisler et al. 1996). We see this trend continue to the outer regions of both M87 and M49.

3.3.2. Virgo A (M87)

The mean M87 GC profiles in Figure 13 show the known difference in the spatial distribution of GCs around galaxies, where the blue GCs have a much more extended profile than do the red GCs (for M87, Côté et al. 2001; Tamura et al. 2006b; Strader et al. 2011; Forte et al. 2012). Due to the low surface densities we probe here (and the complete areal coverage provided by the NGVS), we are able to trace out the GC systems to much larger radii than in most previous studies. The profiles in Figures 13 show the red GC system reaches $\Sigma_{rGC} = 0$ (within the errors) at $r_{maj} \sim 45'$ (~215 kpc) from M87. The blue GC population, however, remains statistically significant all radii, including 2σ above the background at $r_{maj} = 83'$. The mean Σ_{bGC} profile may change slope (to $\Sigma_{bGC} \sim 0.1$–0.2 arcmin^{-2}) at $r_{maj} \sim 50'$–$60'$, although the uncertainties in the profiles at these radii are large. This may be an indication of a more extended population of (largely blue) GCs throughout the Virgo A region; see Section 4.3 for more details.

In Figure 14, we compare our *total* (scaled up by a factor of 2.05 to account for "missed" GCs; see Section 3.1) bGC and rGC number density profiles $\Sigma_{bGC,tot}$ and $\Sigma_{rGC,tot}$ to the red and blue GC profiles from Tamura et al. (2006b). The latter profiles were derived from a 2 deg^2 rectangular region E from M87 toward M59. The bGC profiles are in excellent agreement and the differences in the $\Sigma_{rGC,tot}$ profiles are likely due to the adopted color criteria of the two studies; the $(V - I) = 1.1$ cutoff used by Tamura et al. is significantly redder than our $(g' - i')_o = 0.8$. As a result our Σ_{rGC} profile contains more "blue" GCs as defined by Tamura et al., thus making our rGC profile shallower.

To investigate any spatial variations in the M87 GC system, we fit ellipses to two subsections (NW of M87 along the major

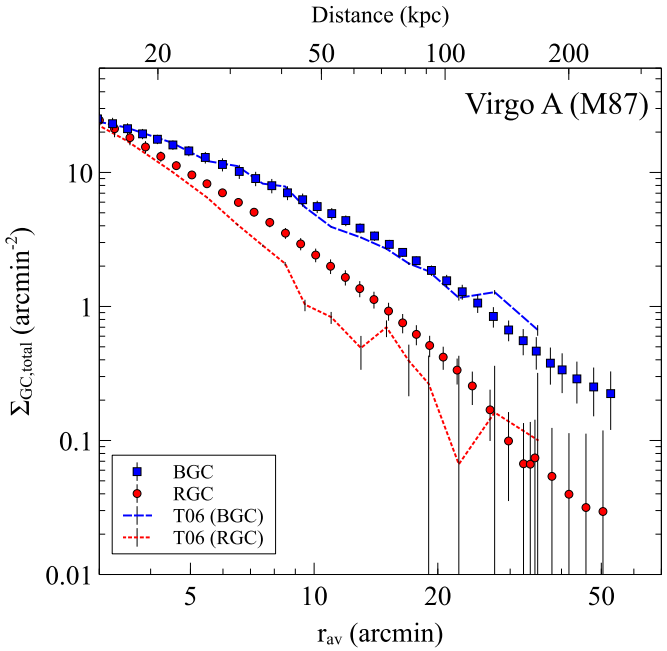

Figure 14. Total number density profiles as a function of average radius $r_{av} = r_{maj}\sqrt{1-\epsilon}$ for the blue (squares; blue in the online version) and red (circles; red in the online version) globular cluster populations for Virgo A(M87), derived from ellipse fits to the adaptive-smoothed maps. Here the plotted number densities $\Sigma_{GC,total}$ have been corrected for those GCs missed in the point-source selection criteria and those objects with $g'_o > 24$. The dashed lines show the total GC number densities for the blue and red GC populations from Tamura et al. (2006b) for a region stretching east from M87 toward M59.

(A color version of this figure is available in the online journal.)

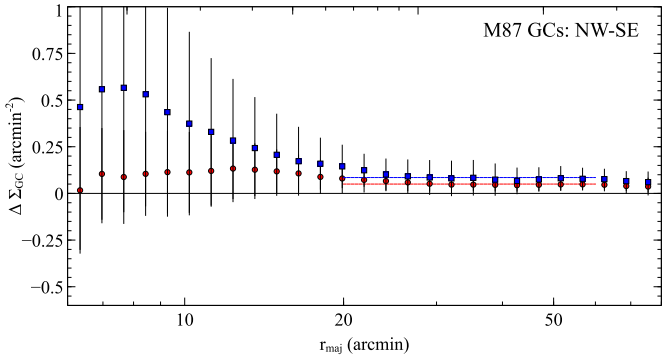

Figure 15. Differences in the surface density profiles $\Delta\Sigma_{bGC}$ (squares; blue in the online version) and $\Delta\Sigma_{rGC}$ (circles; red in the online version) between the NW and SE regions of Virgo A/M87 as a function of the major axis distance from M87. The dashed lines show the mean differences $\Delta\Sigma_{bGC} = 0.085$ arcmin^{-2} and $\Delta\Sigma_{rGC} = 0.05$ arcmin^{-2} from points with $20' < r_{maj} < 60'$.

(A color version of this figure is available in the online journal.)

axis, and toward the SE) of the M87 GC system in the adaptive-smoothed maps. We input the r_{maj}, ϵ and PA values for the mean profiles (derived above) as input to ELLIPSE and derived the surface densities in each half ellipse. Here, we allowed the fitting to continue until 50% of each half ellipse was masked out; the results are plotted as solid lines in Figure 13. In both the blue and red GC profiles, we see slightly larger Σ_{bGC} and Σ_{rGC} values for the NW region than observed in the SE region. To quantify this further, in Figure 15, we plot the differences in the Σ_{bGC} and Σ_{rGC} values ($\Delta\Sigma_{GC} = \Sigma_{GC,NW} - \Sigma_{GC,SE}$) as a function of radius. At most radii there is an excess of GCs in the NW region, although in the inner regions our adopted uncertainties (based on the rms errors of each of the half-ellipse fits) are large enough so that any

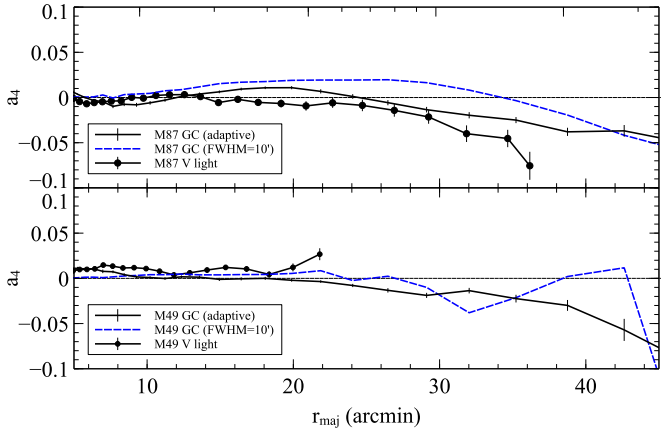

Figure 16. a_4 values for the total GC populations of the Virgo A and B systems plotted as a function of major-axis radius r_{maj}. The solid lines show the a_4 profile derived from ellipse fitting to both the adaptive-smoothed map (black line) and the constant FWHM = 10′ map (dashed line; blue in the online version). For comparison, the black circles show the a_4 profile for M87's light derived from Janowiecki et al. (2010) and for M49's profile from J. C. Mihos et al. (in preparation). The Virgo A GC systems show increasingly boxy isopleths beyond 30–35′ (or 140–170 kpc), inside which the a_4 values are likely affected by the smoothing.

(A color version of this figure is available in the online journal.)

excess is consistent with zero. The differences in both the bGC and rGC profiles are significant (and remarkably constant) at $r_{maj} > 20'$; for $20' < r_{maj} < 60'$ we find $\Delta\Sigma_{bGC} = 0.095 \pm 0.015$ and $\Delta\Sigma_{rGC} = 0.05 \pm 0.01$ (internal uncertainties). While it is possible that some of this excess may be due to the presence of overlapping GC systems from neighboring galaxies (even with the aggressive masking applied before the fits), this feature is observed at smaller radii where such interlopers would be even less apparent. Furthermore, most galaxies that lie within $r_{maj} = 50'$ from M87 have low luminosities and would provide few GCs.

We also note the presence of an enhancement in the GC number density toward the NE, but outside of, the nominal Virgo A GC system described above; this will be discussed further in Section 4.4.

Finally, we examine the deviations from pure elliptical isopleths in the M87 system. Mihos et al. (2005) noted that M87's diffuse envelope appears boxy in its outermost regions, and the total GC map in Figure 9 shows a similar behavior. To quantify this, in Figure 16, we plot the a_4 term (deviations from a perfect ellipse; the percentage of the amplitude of the $\cos(4\theta)$ term in the Fourier expansion) as a function of major axis radius derived from the ellipse fits to both the adaptive smoothed map and the FWHM = 10′ map. In both maps, the a_4 profile becomes progressively more negative (boxy) beyond $r_{maj} \sim 30'$. For comparison, we plot the a_4 profile derived from ellipse fits to the deep *V*-band image of Mihos et al. (2005), showing the increasing boxiness for $r_{maj} > 20'$ for M87's light. While the shapes of the M87 diffuse envelope and the surround GC systems are largely similar, we note that the apparent difference in major axis distance at which these take place. However, as noted above, the effect of circular smoothing on the a_4 profile from our maps at smaller r_{maj} is likely significant.

3.3.3. Virgo B (M49)

Although M49 contains a more prominent system of diffuse shells and streams in its outer regions (Janowiecki et al. 2010) than M87, there is little indication of this in the spatial

Table 1
Globular Clusters in M49 and M87

	$r_{\rm cut}$ (′)	$r_{\rm cut}$ (kpc)[a]	$N_{\rm GC,obs}$[b]	$N_{\rm GC,total}$[c]	$M_{\rm GC,\odot}$[d]
M87 bGC	60′	283	$4730 \pm 110 \pm 60$	$9700 \pm 1070 \pm 120$	$2.3 \pm 0.3 \times 10^9$
M87 rGC	49′	206	$2350 \pm 50 \pm 40$	$4820 \pm 520 \pm 70$	$1.2 \pm 0.1 \times 10^9$
M87 GC				$14520 \pm 1190 \pm 140$	$3.5 \pm 0.4 \times 10^9$
M49 bGC	59′	283	$2700 \pm 80 \pm 100$	$5540 \pm 620 \pm 190$	$1.4 \pm 0.2 \times 10^9$
M49 rGC	49′	206	$1720 \pm 60 \pm 80$	$3530 \pm 400 \pm 160$	$0.8 \pm 0.1 \times 10^9$
M49 GC				$9070 \pm 740 \pm 250$	$2.2 \pm 0.2 \times 10^9$

Notes.
[a] Assuming a Virgo distance $d = 16.5$ Mpc.
[b] Observed number of GCs to $g'_o = 24$.
[c] Total predicted number of GCs with the random errors (correction for the missing GCs) and systematic errors (uncertainties in the background) given.
[d] Total mass of GCs.

distribution of GCs in Figure 12, although (as noted earlier) any small GC populations associated with these features would not appear as significant features in our maps; the six substructures identified by Janowiecki et al. (2010) have a total luminosity of $\sim 7 \times 10^8\ L_\odot$, and would optimistically contribute a total of $\sim$20 GCs brighter than $g_o = 24$. Côté et al. (2003) did, however, see hints of an accretion signature from M49's GC kinematics.

The $\Sigma_{\rm bGC}$, $\Sigma_{\rm rGC}$, and $\Sigma_{\rm GC}$ profiles for M49 are shown in Figure 13. As observed for the M87 profile, the rGC population matches the *V*-band surface brightness profile of the galaxy light quite well and the rGC profile becomes consistent with $\Sigma_{\rm rGC} = 0$ at $r_{\rm maj} \sim 45'$ ($\sim$215 kpc). The more extended bGC population continues to much larger radii and only in the outermost regions (beyond $r_{\rm maj} \sim 60'$) does it appear to flatten off at a level $\Sigma_{\rm bGC} \sim 0.05$ arcmin^{-2}, or 2σ above the background. If this is due to the existence of a more extended cluster-wide GC population, the surface density of this population is lower (roughly half) than that observed around M87.

In Figure 16, we compare the a_4 profile of the Virgo B GC system with that derived from the deep *V*-band Schmidt images from J. C. Mihos et al. (in preparation). While we also see a slight tendency for the Virgo B GC profile to become boxier in the outermost regions, we are only able to compare with the light to $r_{\rm maj} \sim 21'$; however, to this radius, the two profiles appear similar.

3.4. Total Number of GCs in the Virgo Cluster

To derive the total number of GCs throughout the NGVS region, we use the adaptive-smoothed map from Figure 9. There is no statistically significant population of GCs in the outermost regions of the NGVS; the only exception is the (azimuthally non-isotropic; see D'Abrusco et al. 2013) GC system of NGC 4261, which partially lies within the NGVS region. We derive the number of GCs $N_{\rm bGC}$ and $N_{\rm rGC}$ through summing the $\Sigma_{\rm bGC} \times$ (pixel area) and $\Sigma_{\rm rGC} \times$ (pixel area) values. The number of observed blue GCs ($g'_o < 24$) is $N_{\rm bGC} = 21400 \pm 5000$ and that of the red GC population is $N_{\rm rGC} = 11400 \pm 4200$. The uncertainties are based solely on the rms errors of $\Sigma_{\rm bGC}$ and $\Sigma_{\rm rGC}$ from the background fits (the largest source of error), expanded to cover the 106.5 deg^2 area of the NGVS.[27] Correcting for the number of GCs missed by our color, magnitude, and size selection criteria (where 87% of known GCs pass all three criteria), these numbers become $N_{\rm bGC} = 24{,}600 \pm 5800$ and $N_{\rm rGC} = 13{,}100 \pm 4800$ for $g'_o < 24$. Note that we have made no correction for any faint GCs near the M49 core that may have been missed in the SExtractor source lists. We estimated the total number of missing GCs using the number of velocity-confirmed GCs (13) missing in our source catalog. Extrapolating to the entire GC luminosity function, we estimate as many as $\sim$100 GCs (total) are unaccounted for in our estimate. As this is less than 2% of the total population, we have ignored their contribution.

To calculate the *total* GC population within our survey area, we need to correct for those GCs with $g'_o > 24$. The peak of the GC luminosity function lies at $g_{o,\rm ACS} = 23.9 \pm 0.2$, where we have assumed $M_g = -7.2 \pm 0.2$ (Jordán et al. 2007) and $(m - M)_o = 31.1$ from Mei et al. (2007). From the relations in Gwyn (2008), $g'_o \sim g_{\rm ACS} - 0.1$ for $(g - i)$ colors consistent with GCs. Thus the expected peak of the Virgo GCLF is $g'_o = 23.8 \pm 0.2$. Adopting a symmetric Gaussian of $\sigma_{\rm GCLF} = 1.4$ mag[28] for the GCLF, we sample $56\% \pm 6\%$ of the GCLF. Correcting for this, our predicted total number of GCs in the Virgo cluster (bGC and rGC) is $N_{\rm GC,tot} = 67{,}300 \pm 14{,}400$. As a sanity check, $N_{\rm GC}$ values derived from the (fixed kernel) maps in Figure 7 are within 5%; such differences are far below the uncertainties due to the background contamination.

3.5. The M49 and M87 GC Systems

We also use the $\Sigma_{\rm GC}$ profiles from Figure 13 to determine $N_{\rm GC,tot}$ for the individual M49 and M87 GC systems (we did not use the raw $\Sigma_{\rm bGC}$ and $\Sigma_{\rm rGC}$ values from the maps due to the masked regions). For each galaxy, we integrated the mean $\Sigma_{\rm bGC}$ and $\Sigma_{\rm rGC}$ profiles out to a major-axis radius $r_{\rm cut}$. While $r_{\rm cut}$ is difficult to define for the extended bGC population, any uncertainties in $N_{\rm GC,tot}$ due to varying $r_{\rm cut}$ are much smaller than the uncertainties that arise from the correction for GCs below $g'_o = 24$. The results are listed in Table 1.

Our derived values of $N_{\rm GC,total,M87} = 14{,}520 \pm 1190$ (random) $\pm$ 140 (systematic) and $N_{\rm GC,total,M49} = 9070 \pm 740$ (random) $\pm$ 250 (systematic) are slightly larger than that found in most previously published values (e.g., Harris et al. 1998; Rhode & Zepf 2001; Tamura et al. 2006b), although in most cases this is due to the larger extent in which we are able to trace the GC

[27] This number is larger than the 104 deg^2 quoted earlier due to the inclusion of photometry from areas just outside the nominal pointings due to dithering.

[28] While $\sigma_{\rm GCLF}$ scales with galaxy luminosity (Jordán et al. 2007), this will not have a significant effect on our results due to our magnitude cutoff lying near the GCLF peak.

systems[29]. When we consider the total number of GCs within smaller radii, our results are consistent with previous works. Our values are consistent with $N_{GC,M87} = 14{,}660 \pm 891$ and $N_{GC,M49} = 7813 \pm 830$ derived by Peng et al. (2008) via the integration of the best-fitting Sérsic profiles to their GC profiles to larger radii.

4. DISCUSSION

4.1. The Virgo Cluster-wide Distribution of Globular Clusters

Our results indicate that the Virgo cluster has a large GC population spread out over a wide area of the NGVS region. The GCs are distributed, unsurprisingly, much like that of the early-type galaxies in Virgo. The lowest-resolution (FWHM = 30′) map in Figure 7 shows the extent of the (both red and blue) GCs throughout Virgo, down to a 3σ limit $\Sigma_{GC} = 0.084$ arcmin^{-2} (or a total GC number density $\Sigma_{GC,tot} = 0.17$ arcmin^{-2}), where GCs are seen to extend to large distances from the large galaxies. We see GCs ∼1.°75–2.°5 (500–700 kpc) from M87; for the M49 region, we see GCs extend out to at least = 1.°25 (∼350 kpc). The populous GC systems of M49 and M87 together comprise 35% ± 7% of the total Virgo GC population, even though those galaxies contain only ∼8% of the total *B* luminosity of the Virgo cluster. The majority of these GCs are distributed (albeit irregularly) around M87, the center of the most massive subcluster in Virgo. As a result of this, the bulk of the GCs also appear to follow the principal axis of the cluster (West & Blakeslee 2000) from the M60 subcluster, westward through M87 to beyond M84/86.

The distribution of Virgo's GC population is not only similar to that of the diffuse light present in the cluster, but also closely matches that of the hot X-ray intracluster gas (also noted by Lee et al. 2010). In Figure 17, we compare our FWHM = 30′ map contours with the X-ray image from Böhringer et al. (1994), derived from the *ROSAT* All-Sky Survey. The dashed X-ray contour shows the close correspondence between the X-rays and the GCs down to the 3σ level of the latter. Due to the limits in the GC number densities due to our background, we cannot effectively compare the two distributions at larger distances where there is still significant X-ray emission.

We not only confirm that the blue GCs in Virgo have a more extended distribution than the red GCs, but that the red GC populations around both M49 and M87 largely disappear (to the limits of our data) at galactocentric distances $r > 215$ kpc. *Beyond this, the majority of the GC candidates are (metal-poor) bGCs*. That we have (largely) metal-poor GCs lying several hundreds of kiloparsecs from the center of Virgo does suggest some or most of them are part of the intracluster component of Virgo. We discuss the evidence for such an extended population below. This would indicate that the bulk of the GCs at such large distances from the primary galaxies had originated either in dwarf galaxies (which have preferentially blue GCs, Peng et al. 2008; see also Schuberth et al. 2010) or from the outer regions of larger galaxies, where fewer red GCs are located. It is important to note a *small* population of rGCs could certainly exist at larger radii; an extended GC population composed of ∼10% ± 10% red GCs (Peng et al. 2011, found ∼20% red GCs in the Coma cluster core) could still be present within the uncertainties in our maps.

[29] Forte et al. (2012) derive a larger N_{GC} value that we do. We are unsure of the reason for this discrepancy. While our values may be slightly underestimated due to a small number of GCs being smoothed to larger radii, this alone cannot explain the difference.

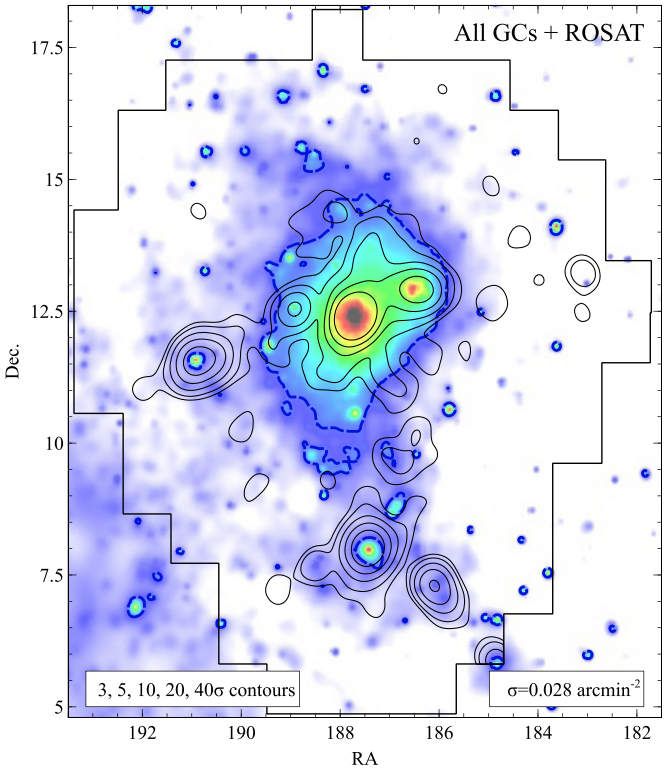

Figure 17. FWHM = 30′ smoothed map contours (3σ, 5σ, 10σ, 20σ, 40σ above the background) plotted over the *ROSAT* All-Sky Survey image of Virgo in the 0.5–2.0 keV range (Böhringer et al. 1994). The dashed line denotes the X-ray level at a value $\sim 11\sigma$ above the background, based on inspection of their Figure 1.

(A color version of this figure is available in the online journal.)

4.2. Comparison with Lee et al. (2010)

Lee et al. (2010) were the first to study the cluster-wide distribution of Virgo's GC population through the use of SDSS photometry and using an adaptive smoothing method similar to that applied here. They found that GCs are distributed over a large region of Virgo, with the densest GC regions (with both blue and red GCs) around the dominant galaxies in many Virgo subclusters, including M87, M84/86, M60, and M49. The red GCs only appear to exist around these major subgroups. The blue GCs are much more extended and fill the region in Virgo along its principal axis.

The NGVS photometry we use probes much fainter limits to that possible in that study (∼13% of the GCLF compared to 56% ± 6% in our study), allowing us to detect more than four times as many GCs. More importantly, that we use more GCs to define our maps not only allows enables us to probe scales of a few arcminutes, but also facilitates a better characterization of the background noise level.

A comparison between Figures 7 and 2(a) from Lee et al. shows generally good agreement, down to similar number densities. Their lowest contour corresponds to (after correction for different photometric depths) $\Sigma_{GC} \sim 0.055$ arcmin^{-2}, or the 2σ level in the FWHM = 30′ map, where we find a similar distribution of GCs around M84/M86/M87/M89, M49, and M60. However, there are some notable differences between the maps. We are able to trace out the GC systems for all galaxies in 'Markarian's Chain' (Markarian 1961) that extend north of M87 out to NGC 4477. For this reason (and the detection of M88's GC system), we find GCs extending over 2 degrees north

of M87; this is a feature seen in the X-ray map in Figure 17, but not in L10. Similarly, a large, diffuse GC region west of M87 in the L10 map but not in the X-ray maps is not seen in our maps at all, although the prominent GC system of NGC 4168, not a Virgo cluster member, does appear in this area.

4.3. Cluster S_N and GC Formation Efficiency

Our value of $N_{\rm GC,tot}$ is the first true measurement of the GC population over an entire galaxy cluster. Thus we are able to investigate the *cluster* specific frequency $S_{N,\rm CL}$ as an extension of the usual S_N (number of GCs per unit luminosity) defined for individual galaxies (Harris & van den Bergh 1981). To derive the total luminosity L_V of the Virgo Cluster, we used the B_T magnitudes for all VCC galaxies that are (1) confirmed or probable members of the Virgo cluster and (2) located within the NGVS footprint. We adopted colors $(B-V) = 0.95 \pm 0.10$ for all galaxies classified E/EI/ES (from Section 3.2 and Figure 10) and $(B-V) = 0.70 \pm 0.20$ for all other galaxies. These values (and their assumed errors) are based on inspection of colors from the RC3 (e.g., Corwin et al. 1994) for the brighter early and late-type galaxies. From these, we derive a total $L_V = 1.84 \pm 0.16 \times 10^{12}\ L_\odot$, for Virgo's galaxies. To account for any diffuse intracluster light in Virgo that is not included in any VCC magnitudes, we apply an additional (albeit very uncertain) luminosity of 10%±10% based on studies of Virgo's intracluster RGB stars and PNe (e.g., Durrell et al. 2002; Feldmeier et al. 2004a; Castro-Rodriguéz et al. 2009). The total V-band luminosity of the Virgo Cluster is $L_V = 2.02 \pm 0.24 \times 10^{12}\ L_\odot$, or $M_V = -25.95 \pm 0.15$ assuming $M_{V,\odot} = +4.81$. We thus derive

$$S_{N,\rm CL} = 2.8 \pm 0.7$$

for the Virgo cluster, a value similar to that of elliptical galaxies. Ignoring the uncertain ICL light fraction would yield a slightly larger $S_{N,\rm CL} = 3.1 \pm 0.7$.

Many studies (Blakeslee et al. 1997; Blakeslee 1999; Spitler & Forbes 2009; Georgiev et al. 2010; Hudson et al. 2014) have shown that the ratio of the GC mass to the total (baryonic+dark matter) mass of galaxies (or GC formation efficiency $\epsilon_t = M_{\rm GC}/M_{\rm total}$) is similar for galaxies over a wide range of morphology and luminosity, where $\epsilon_t \sim 4$–6×10^{-5} (Spitler & Forbes 2009; Georgiev et al. 2010; Hudson et al. 2014).[30] McLaughlin (1999b) found a similar relation relating $M_{\rm GC}$ to the total *baryonic* mass (stars + intracluster gas) in galaxies: $\epsilon_b = M_{\rm GC}/M_{\rm baryon} \sim 0.0026$. These relationships may reflect the early formation of the GCs in proportion to total available mass before feedback mechanisms become effective in shutting off future star formation. Alamo-Martínez et al. (2013) noted, however, that such formation efficiencies are (necessarily) dependent on the radius out to which the various masses are derived and found both ϵ_b and ϵ_t to decrease with radius in the massive galaxy cluster A1689.

It is interesting to see if the scaling of GCs with mass for individual galaxies holds for the Virgo cluster as a whole. Assuming an average GC mass $M = 2.4 \times 10^5\ M_\odot$ (McLaughlin 1999b), the total mass of GCs in Virgo is $M_{\rm GC} = 1.6 \pm 0.3 \times 10^{10}\ M_\odot$. For the baryonic mass, we combine the intracluster gas mass of the M87, M49, and M86 groups $M_{\rm gas} = 2 \times 10^{13}\ M_\odot$ (Schindler et al. 1999) with the total stellar mass $M_* = 8.1 \times 10^{12}\ M_\odot$, found by assuming $M/L_V = 4$ for old, metal-rich populations (Alamo-Martínez et al. 2013). Thus for a total Virgo baryonic mass of $2.8 \times 10^{13}\ M_\odot$, we find a baryonic GC formation efficiency

$$\epsilon_b = 5.7 \pm 1.1 \times 10^{-4}.$$

This value is lower than $\epsilon_b = 2.6 \times 10^{-3}$ from McLaughlin (1999a) and $\epsilon_b = 9.5 \times 10^{-4}$ from Alamo-Martínez et al. (2013), although these values are derived at radii of 100 kpc and 400 kpc from the central galaxy, while our results are for the region within Virgo's virial radius (∼1.5 Mpc). For the total cluster mass, we combine the dark matter halo masses of the Virgo A and B subclusters from Ferrarese et al. (2012), based on McLaughlin (1999a), and the total mass for the M86 subcluster from Schindler et al. (1999), to get $M_{\rm Virgo} = 5.5 \times 10^{14}\ M_\odot$. Thus we derive

$$\epsilon_t = 2.9 \pm 0.5 \times 10^{-5},$$

where the error is based on the uncertainty in $M_{\rm GC,tot}$ only. This result is slightly lower than previously derived galactic values of $\epsilon_t = 4.2 \times 10^{-5}$ (Spitler & Forbes 2009) and $\epsilon_t = 3.9 \pm 0.9 \times 10^{-5}$ (Hudson et al. 2014), but is well within the observed spread seen in both studies, where many galaxies have $\epsilon_t \sim 1$–10×10^{-5}. Moreover, given the decline in ϵ_t with radius (Alamo-Martínez et al. 2013), there should be some limited region within Virgo over which ϵ_t matches the mean for individual galaxies, although the global value is lower. It is important to note that our values of ϵ_b and ϵ_t are largely independent of our assumed correction for Virgo's ICL, as Virgo's stellar mass is a small fraction of the baryonic and total masses.

4.4. Virgo's Extended Stellar Populations

The extended spatial extent of Virgo's GC population and its striking similarity to the distribution of the intracluster gas suggests that some GCs *must* be members of the intracluster medium. Unfortunately, with spatial information alone, it is difficult to distinguish between "galactic" GCs and IGCs; see West et al. (2011) for a cautionary discussion of IGCs in A1185. A classic definition of intergalactic populations are regions where the surface brightness/number density profile of a galaxy changes slope in the outer regions, suggesting an additional stellar population. The total blue GC number densities in the outermost regions of Virgo A and B are at the $\Sigma_{\rm bGC,tot} \sim 0.2$ arcmin^{-2} and $\Sigma_{\rm bGC,tot} \sim 0.1$ arcmin^{-2}, respectively. These values are consistent with the broad limits on any IGC population by Tamura et al. (2006b). That these values are only 2–3σ above our background level reduces our ability to effectively model the IGC population as merely an excess of objects above a one-dimensional profile of the galactic GC populations (see Figure 13); indeed, we only see possible evidence for an inflection point at $r_{\rm maj} \sim 50'$–$60'$ (240–290 kpc) in the $\Sigma_{\rm bGC}$ profiles.

Any IGCs superimposed on the large galaxies themselves would only become obvious through velocity information derived from spectroscopic follow-up studies, otherwise they appear as if they were part of the galactic GC system.[31] As noted in Section 3.3.2, it is possible to find extra components through

[30] We have changed the results from Spitler & Forbes (2009) to reflect the median GC mass we have adopted.

[31] This situation is not unique to IGCs, as there have been many definitions used as to what constitutes the intracluster component in diffuse light studies (e.g., Dolag et al. 2010; Rudick et al. 2011).

their spatial distribution alone. Modeling (and masking) the GC systems around individual Virgo galaxies (Peng et al. 2011, for the Coma cluster) is beyond the scope of this work and such a task will (necessarily) be left to future studies using multiple colors (e.g., Muñoz et al. 2014) and spectroscopy to significantly reduce the background contamination.

With these caveats in mind, we have found a small spatial asymmetry in the GC number densities within the M87 system (at $r_{\rm maj} < 50'$). We also find possible evidence for an excess in the GC surface densities NE of M87 (labeled "NE" in Figure 9), which lies outside the M87 GC system but in a region with only a few low luminosity dwarf galaxies. While this latter feature lies $\sim 2.5\sigma$ above the nominal M87 GC system in our maps (5σ above the mean background), it is something to be investigated in future studies. Both of these spatial features could plausibly be due to the presence of an extended intracluster GC population. Recent dynamical studies of GCs in the M87 region have shown additional substructures within 100 kpc from the center of M87 (Romanowsky et al. 2012; Zhu et al. 2014). While it is possible that the NW/SE asymmetry we see is related to either of these features, the GC excess we see lies further ($r_{\rm maj} > 20'$–$50' = 100$–250 kpc) from M87 than the kinematic features. The presence of both spatial and kinematic substructure in the GC populations strengthens the case that the production of the ICL (including the liberation of the intracluster stellar populations) is an ongoing process that continues to the present time.

That most of the spatial and kinematic substructures (thus far) are located toward M87's NW major axis may not be a coincidence. The diffuse optical light observed by Mihos et al. (2005), Janowiecki et al. (2010), the kinematics of PNe NW of M87 from Doherty et al. (2009), and the presence of GCs extending over 700 kpc NW of M87 are all suggestive of an intracluster population that is not centered on M87. Although this has been attributed to the presence of a significant diffuse light component around M86 (and not M87) by Doherty et al. (2009), the wealth of (tidal) substructure around M87 would suggest a larger extended GC population in the Virgo A region. This can only be tested by much larger spectroscopic samples in this region of the Virgo cluster.

A useful comparison can be made between the number density profiles of the GCs in the Virgo A region with that of the PNe. A spectroscopic study of a small number of PNe in the Virgo core by Doherty et al. (2009) suggests that PNe outside $r_{\rm maj} \sim 210$ kpc[32] from M87 exhibit kinematics expected for an intracluster population rather than that of objects bound to M87's halo. In Figure 13, we overlay the surface density profile of a photometrically selected sample of PNe from Longobardi et al. (2013) on our mean GC (bGC+rGC) profile. Although the uncertainties in the PNe profile are not explicitly given (the PNe profile is very sensitive to the background corrections applied), there is excellent agreement in the profiles between the two populations, even though the GCs and the PNe may not necessarily track the same stellar populations. While Longobardi et al. (2013) attribute their excess of PNe (compared to that of the galaxy light) to the combination of an M87 halo and an ICL stellar population (the latter of which has a more metal-poor composition), it is possible that some of their ICL component may be related to the blue GC component of M87's halo.

[32] We have corrected the Doherty et al. (2009) circular-averaged radius $R = 149$ kpc to a major-axis radius assuming $\epsilon = 0.43$ and using $d = 16.5$ Mpc.

4.5. Virgo's Dynamical History

The wealth of both spatial and kinematic substructure in the galaxy population of the Virgo Cluster (e.g., Binggeli et al. 1987, 1993; Mei et al. 2007; Paudel et al. 2013) is evidence the cluster is not in a fully relaxed state. Furthermore, the observations of Virgo's extended stellar populations (GCs, PNe, diffuse light) discussed above allow a qualitative discussion on the dynamical state(s) of the Virgo Cluster as a whole. Virgo is the first cluster where the spatial distribution of the entire GC system can be compared to both the cluster-wide intracluster gas and the galaxy population (e.g., Lee et al. 2010). The 2D distribution of Virgo's GCs over a larger scale largely follows the irregular distribution of the galaxies. This result, combined with the spatial and kinematic substructures observed in the stellar populations both within and outside Virgo galaxies (e.g., Mihos et al. 2005; Doherty et al. 2009; Janowiecki et al. 2010; Lee et al. 2010; Romanowsky et al. 2012; Zhu et al. 2014), is a clear indication of the recent (and ongoing) ICL/IGC production. Rudick et al. (2009) suggest that build-up of the ICL is through continual, though episodic processes that have occurred over a large fraction of a Hubble time. Our results are consistent with this picture. There are (related) suggestions that a large fraction of the current ICL was pre-processed by stripping from galaxies in the group environment before their eventual infall into the cluster environment (Mihos 2004; Rudick et al. 2006). While we cannot directly test this idea here (as we are not studying the group environments at the lowest level), that the smaller subclusters in Virgo (e.g., M49, M60) show less evidence for any IGC population (based on the extent of the bGC populations around M49 and M60 in Figure 7) suggests that ICL production around these (less massive) subclusters is perhaps still in its earliest stages. Forthcoming *K*-band imaging of Virgo (e.g., the methods from Muñoz et al. 2014) promises to reduce the background contamination further, and allows us to trace the GC population to lower levels than possible here, and would facilitate comparisons with the predictions of cosmological models (e.g., Moore et al. 2006). In contrast, the similarity in the spatial distributions of the intracluster gas and GCs around M87 suggests that the two components have similar dynamical histories. This would indicate that some fraction of the IGC population in Virgo's largest subcluster was liberated early on, or at least at early enough times to allow for partial virial equilibrium. It will be interesting to compare the large-scale GC and X-ray distributions in other clusters in order to determine if a similar correspondence holds in systems of different masses and/or dynamical states and if we can directly trace the build up of the ICL component through the GCs.

5. SUMMARY

We have used $g'i'$ photometry for point sources from the NGVS to extract the population of GCs throughout the survey area. We show the following.

1. Number density maps of Virgo's GCs show a complex 2D structure surrounding the large early-type galaxies in the cluster. Many of the GCs are located near the core of the Virgo cluster, the massive subcluster Virgo A. The Virgo cluster contains a total population of $67,300 \pm 14,400$ GCs, with a significant fraction ($\sim$35%) of these lying within the GC systems of M87 and M49 alone. The resulting cluster-wide specific frequency $S_{N,\rm CL}$ is 2.8 ± 0.7, and we derive a GC-to-baryonic mass ratio $\epsilon_b = 5.7 \pm 1.1 \times 10^{-4}$ and a

total GC mass ratio $\epsilon_t = 2.9 \pm 0.5 \times 10^{-5}$ within Virgo's virial radius.

2. The GC systems of M87 and M49 are very similar in shape and extent to the diffuse light that is known to surround both galaxies. The M87 GC system, in particular, shows the same "boxy" isopleths as seen in the diffuse light in the outer regions of M87, indicative of a common origin.
3. The GC systems in both the Virgo A (M87) and Virgo B (M49) subclusters extend to large radii. The red (metal-rich) GCs are found to follow the galaxy light and are seen to extend as far as ∼215 kpc from the central galaxies; beyond this distance, the red GC population is consistent with zero. The blue (metal-poor) GC population has a shallow distribution and extends to much larger distances with significant populations of GCs still present (with total number densities $\Sigma_{GC} \sim 0.1$–0.2 arcmin^{-2}) 400 kpc from the central galaxies. If some (or all) of the GCs at these radii are "intracluster" GCs, this suggests such a population is largely comprised of metal-poor objects and is suggestive of an origin from either dwarf galaxies or preferentially removed from the outer regions of larger galaxies. The gravitational processes that have liberated these GCs from their original galaxies continue to the present day.
4. We have found a small asymmetry in the M87 GC system, where an observed excess of GCs at $\Sigma_{GC,tot} \sim 0.2$ arcmin^{-2} is observed toward the NW of M87. Whether this feature is caused by a population of GCs that is offset from, but superposed on, the M87 GC system or is partially related to kinematic substructures detected within the M87 GC system itself (Romanowsky et al. 2012; Zhu et al. 2014) cannot be clearly defined from our data. The increasing complexity of the M87 region (both spatially and kinematically) provides strong evidence of the recent and continuing processes of galactic accretion throughout the Virgo core.
5. The GCs surrounding M87 have a similar spatial distribution to that of the (relaxed) intracluster gas in the region, suggesting that the build up of the extended GC population began at an epoch early enough for some of the GC population to be in a similarly relaxed state. This is consistent with the slow, gradual build up of the outer regions of BCGs, including the ICL.

The authors thank Hans Böhringer for the use of the *ROSAT* X-ray data, and the anonymous referee who made numerous useful suggestions to improve this paper. P.R.D. gratefully acknowledges support from NSF grant AST-0908377. P.R.D. thanks John Feldmeier and Myung Gyoon Lee for useful discussions throughout the writing of this paper; Jay Strader for making his M87 GC catalog available before publication; and the Department of Astronomy at Case Western Reserve University, where parts of this paper were written. J.C.M. has been supported through NSF grants AST-0607526 and AST-1108964. C.L. acknowledges support from the National Natural Science Foundation of China (grant Nos. 11203017, 11125313, and 10973028). P.A.D. acknowledges support from Agence Nationale de la Recherche (ANR10-BLANC-0506-01).

The NGVS team owes a debt of gratitude to the director and the staff of the Canada–France–Hawaii Telescope, whose dedication, ingenuity, and expertise have helped make the survey a reality. This work is supported in part by the French Agence Nationale de la Recherche (ANR) Grant Programme Blanc VIRAGE (ANR10-BLANC-0506-01), and by the Canadian Advanced Network for Astronomical Research (CANFAR), which has been made possible by funding from CANARIE under the Network-Enabled Platforms program. This research used the facilities of the Canadian Astronomy Data Centre operated by the National Research Council of Canada with the support of the Canadian Space Agency. The authors further acknowledge use of the NASA/IPAC Extragalactic Database (NED), which is operated by the Jet Propulsion Laboratory, California Institute of Technology, under contract with the National Aeronautics and Space Administration, and the HyperLeda database (http://leda.univ-lyon1.fr).

Facility: CFHT

REFERENCES

Abadi, M. G., Navarro, J. F., & Steinmetz, M. 2006, MNRAS, 365, 747
Abell, G. O., Corwin, H. G., Jr., & Olowin, R. P. 1989, ApJS, 70, 1
Aguerri, J. A. L., Gerhard, O. E., Arnaboldi, M., et al. 2005, AJ, 129, 2585
Alamo-Martínez, K. A., Blakeslee, J. P., Jee, M. J., et al. 2013, ApJ, 775, 20
An, D., Beers, T. C., Johnson, J. A., et al. 2013, ApJ, 763, 65
Arnaboldi, M., Gerhard, O., Aguerri, J. A. L., et al. 2004, ApJL, 614, L33
Ashman, K. M., & Zepf, S. E. (ed.) 1998, Globular Cluster Systems (Cambridge: Cambridge Univ. Press)
Bassino, L. P., Cellone, S. A., Forte, J. C., & Dirsch, B. 2003, A&A, 399, 489
Bassino, L. P., Faifer, F. R., Forte, J. C., et al. 2006, A&A, 451, 789
Bekki, K., & Yahagi, H. 2006, MNRAS, 372, 1019
Belokurov, V., Zucker, D. B., Evans, N. W., et al. 2006, ApJL, 642, L137
Bergond, G., Athanassoula, E., Leon, S., et al. 2007, A&A, 464, L21
Bertin, E., & Arnouts, S. 1996, A&AS, 117, 393
Binggeli, B., Popescu, C. C., & Tammann, G. A. 1993, A&AS, 98, 275
Binggeli, B., Sandage, A., & Tammann, G. A. 1985, AJ, 90, 1681
Binggeli, B., Tammann, G. A., & Sandage, A. 1987, AJ, 94, 251
Blakeslee, J. P. 1999, AJ, 118, 1506
Blakeslee, J. P., Cho, H., Peng, E. W., et al. 2012, ApJ, 746, 88
Blakeslee, J. P., Jordán, A., Mei, S., et al. 2009, ApJ, 694, 556
Blakeslee, J. P., Tonry, J. L., & Metzger, M. R. 1997, AJ, 114, 482
Böhringer, H., Briel, U. G., Schwarz, R. A., et al. 1994, Natur, 368, 828
Bonaca, A., Jurić, M., Ivezić, Ž., et al. 2012, AJ, 143, 105
Bressan, A., Marigo, P., Girardi, L., et al. 2012, MNRAS, 427, 127
Brodie, J. P., Romanowsky, A. J., Strader, J., & Forbes, D. A. 2011, AJ, 142, 199
Brodie, J. P., & Strader, J. 2006, ARA&A, 44, 193
Burbidge, E. M., & Sandage, A. 1958, ApJ, 127, 527
Burke, C., Collins, C. A., Stott, J. P., & Hilton, M. 2012, MNRAS, 425, 2058
Busko, I. C. 1996, in ASP Conf. Ser. 101, Astronomical Data Analysis Software and Systems V, ed. G. H. Jacoby & J. Barnes (San Francisco, CA: ASP), 139
Castro-Rodriguéz, N., Arnaboldi, M., Aguerri, J. A. L., et al. 2009, A&A, 507, 621
Coenda, V., Muriel, H., & Donzelli, C. 2009, ApJ, 700, 1382
Cohen, J. G. 2000, AJ, 119, 162
Collins, C. A., Stott, J. P., Hilton, M., et al. 2009, Natur, 458, 603
Conroy, C., Wechsler, R. H., & Kravtsov, A. V. 2007, ApJ, 668, 826
Corwin, H. G., Jr., Buta, R. J., & de Vaucouleurs, G. 1994, AJ, 108, 2128
Côté, P., Blakeslee, J. P., Ferrarese, L., et al. 2004, ApJS, 153, 223
Côté, P., McLaughlin, D. E., Cohen, J. G., & Blakeslee, J. P. 2003, ApJ, 591, 850
Côté, P., McLaughlin, D. E., Hanes, D. A., et al. 2001, ApJ, 559, 828
Cui, W., Murante, G., Monaco, P., et al. 2014, MNRAS, 437, 816
Cypriano, E. S., Sodré, L., Jr., Campusano, L. E., Dale, D. A., & Hardy, E. 2006, AJ, 131, 2417
D'Abrusco, R., Fabbiano, G., Strader, J., et al. 2013, ApJ, 773, 87
Davies, J. I., Bianchi, S., Cortese, L., et al. 2012, MNRAS, 419, 3505
Doherty, M., Arnaboldi, M., Das, P., et al. 2009, A&A, 502, 771
Dolag, K., Murante, G., & Borgani, S. 2010, MNRAS, 405, 1544
Dubinski, J. 1998, ApJ, 502, 141
Duffau, S., Zinn, R., Vivas, A. K., et al. 2006, ApJL, 636, L97
Durrell, P. R., Ciardullo, R., Feldmeier, J. J., Jacoby, G. H., & Sigurdsson, S. 2002, ApJ, 570, 119
Feigelson, E. D., & Babu, G. J. 1992, ApJ, 397, 55
Feldmeier, J. J., Ciardullo, R., & Jacoby, G. H. 1998, ApJ, 503, 109
Feldmeier, J. J., Ciardullo, R., Jacoby, G. H., & Durrell, P. R. 2004a, ApJ, 615, 196
Feldmeier, J. J., Mihos, J. C., Morrison, H. L., et al. 2004b, ApJ, 609, 617
Ferguson, H. C., Tanvir, N. R., & von Hippel, T. 1998, Natur, 391, 461

Ferrarese, L., Côté, P., Cuillandre, J.-C., et al. 2012, ApJS, 200, 4
Firth, P., Drinkwater, M. J., & Karick, A. M. 2008, MNRAS, 389, 1539
Forte, J. C., Martinez, R. E., & Muzzio, J. C. 1982, AJ, 87, 1465
Forte, J. C., Vega, E. I., & Faifer, F. 2012, MNRAS, 421, 635
Gal-Yam, A., Maoz, D., Guhathakurta, P., & Filippenko, A. V. 2003, AJ, 125, 1087
Geisler, D., Lee, M. G., & Kim, E. 1996, AJ, 111, 1529
Georgiev, I. Y., Puzia, T. H., Goudfrooij, P., & Hilker, M. 2010, MNRAS, 406, 1967
Gerhard, O., Arnaboldi, M., Freeman, K. C., et al. 2007, A&A, 468, 815
Gnedin, O. Y. 2003, ApJ, 589, 752
Gonzalez, A. H., Zabludoff, A. I., & Zaritsky, D. 2005, ApJ, 618, 195
Gregg, M. D., Drinkwater, M. J., Evstigneeva, E., et al. 2009, AJ, 137, 498
Grillmair, C. J., Freeman, K. C., Bicknell, G. V., et al. 1994, ApJL, 422, L9
Gwyn, S. D. J. 2008, PASP, 120, 212
Hanes, D. A., Côté, P., Bridges, T. J., et al. 2001, ApJ, 559, 812
Harris, W. E. 1986, AJ, 91, 822
Harris, W. E. 1991, ARA&A, 29, 543
Harris, W. E. 2001, Star Clusters. Saas-Fee Advanced Courses, Vol. 28 (Berlin: Springer), 223
Harris, W. E. 2009a, ApJ, 699, 254
Harris, W. E. 2009b, ApJ, 703, 939
Harris, W. E., Harris, G. L. H., & McLaughlin, D. E. 1998, AJ, 115, 1801
Harris, W. E., Kavelaars, J. J., Hanes, D. A., Pritchet, C. J., & Baum, W. A. 2009, AJ, 137, 3314
Harris, W. E., & van den Bergh, S. 1981, AJ, 86, 1627
Hudson, M. J., Harris, G. L., & Harris, W. E. 2014, ApJL, 787, L5
Janowiecki, S., Mihos, J. C., Harding, P., et al. 2010, ApJ, 715, 972
Jedrzejewski, R. I. 1987, MNRAS, 226, 747
Jordán, A., McLaughlin, D. E., Côté, P., et al. 2007, ApJS, 171, 101
Jordán, A., Peng, E. W., Blakeslee, J. P., et al. 2009, ApJS, 180, 54
Jordán, A., West, M. J., Côté, P., & Marzke, R. O. 2003, AJ, 125, 1642
Jurić, M., Ivezić, Ž., Brooks, A., et al. 2008, ApJ, 673, 864
Kartha, S. S., Forbes, D. A., Spitler, L. R., et al. 2014, MNRAS, 437, 273
Kim, H.-S., Yoon, S.-J., Sohn, S. T., et al. 2013, ApJ, 763, 40
Kissler-Patig, M., Grillmair, C. J., Meylan, G., et al. 1999, AJ, 117, 1206
Krick, J. E., & Bernstein, R. A. 2007, AJ, 134, 466
Krick, J. E., Bernstein, R. A., & Pimbblet, K. A. 2006, AJ, 131, 168
Kundu, A., Whitmore, B. C., Sparks, W. B., et al. 1999, ApJ, 513, 733
Laporte, C. F. P., White, S. D. M., Naab, T., & Gao, L. 2013, MNRAS, 435, 901
Lee, M. G., & Kim, E. 2000, AJ, 120, 260
Lee, M. G., Kim, E., & Geisler, D. 1998, AJ, 115, 947
Lee, M. G., Park, H. S., & Hwang, H. S. 2010, Sci, 328, 334
Longobardi, A., Arnaboldi, M., Gerhard, O., et al. 2013, A&A, 558, A42
Marigo, P., Girardi, L., Bressan, A., et al. 2008, A&A, 482, 883
Markarian, B. E. 1961, AJ, 66, 555
McLaughlin, D. E. 1999a, ApJL, 512, L9
McLaughlin, D. E. 1999b, AJ, 117, 2398
McLaughlin, D. E., Harris, W. E., & Hanes, D. A. 1994, ApJ, 422, 486
Mei, S., Blakeslee, J. P., Côté, P., et al. 2007, ApJ, 655, 144
Mihos, J. C. 2004, in IAU Symp. 217, Recycling Intergalactic and Interstellar Matter, ed. P.-A. Duc, J. Braine, & E. Brinks (San Francisco, CA: ASP), 390
Mihos, J. C., Harding, P., Feldmeier, J., & Morrison, H. 2005, ApJL, 631, L41
Mihos, J. C., Harding, P., Rudick, C. S., & Feldmeier, J. J. 2013, ApJL, 764, L20
Monaco, P., Murante, G., Borgani, S., & Fontanot, F. 2006, ApJL, 652, L89
Moore, B., Diemand, J., Madau, P., Zemp, M., & Stadel, J. 2006, MNRAS, 368, 563
Muñoz, R. P., Puzia, T. H., Lançon, A., et al. 2014, ApJS, 210, 4
Murante, G., Arnaboldi, M., Gerhard, O., et al. 2004, ApJL, 607, L83
Murante, G., Giovalli, M., Gerhard, O., et al. 2007, MNRAS, 377, 2
Muzzio, J. C. 1986, ApJ, 301, 23
Muzzio, J. C. 1987, PASP, 99, 245
Muzzio, J. C., Martinez, R. E., & Rabolli, M. 1984, ApJ, 285, 7
Naab, T., Johansson, P. H., & Ostriker, J. P. 2009, ApJL, 699, L178
Niederste-Ostholt, M., Belokurov, V., Evans, N. W., & Peñarrubia, J. 2010, ApJ, 712, 516
Oser, L., Ostriker, J. P., Naab, T., Johansson, P. H., & Burkert, A. 2010, ApJ, 725, 2312
Park, H. S., Lee, M. G., & Hwang, H. S. 2012, ApJ, 757, 184
Paudel, S., Duc, P.-A., Côté, P., et al. 2013, ApJ, 767, 133
Peng, E. W., Ferguson, H. C., Goudfrooij, P., et al. 2011, ApJ, 730, 23
Peng, E. W., Jordán, A., Côté, P., et al. 2006, ApJ, 639, 95
Peng, E. W., Jordán, A., Côté, P., et al. 2008, ApJ, 681, 197
Purcell, C. W., Bullock, J. S., & Zentner, A. R. 2007, ApJ, 666, 20
Puzia, T. H., Paolillo, M., Goudfrooij, P., et al. 2014, ApJ, 786, 78
Puzia, T. H., Zepf, S. E., Kissler-Patig, M., et al. 2002, A&A, 391, 453
Rhode, K. L., & Zepf, S. E. 2001, AJ, 121, 210
Rhode, K. L., & Zepf, S. E. 2004, AJ, 127, 302
Romanowsky, A. J., Strader, J., Brodie, J. P., et al. 2012, ApJ, 748, 29
Rudick, C. S., Mihos, J. C., Frey, L. H., & McBride, C. K. 2009, ApJ, 699, 1518
Rudick, C. S., Mihos, J. C., & McBride, C. 2006, ApJ, 648, 936
Rudick, C. S., Mihos, J. C., & McBride, C. K. 2011, ApJ, 732, 48
Ruszkowski, M., & Springel, V. 2009, ApJ, 696, 1094
Ryan, S. G., & Norris, J. E. 1991, AJ, 101, 1865
Sand, D. J., Graham, M. L., Bildfell, C., et al. 2011, ApJ, 729, 142
Schindler, S., Binggeli, B., & Böhringer, H. 1999, A&A, 343, 420
Schlegel, D. J., Finkbeiner, D. P., & Davis, M. 1998, ApJ, 500, 525
Schuberth, Y., Richtler, T., Bassino, L., & Hilker, M. 2008, A&A, 477, L9
Schuberth, Y., Richtler, T., Hilker, M., et al. 2010, A&A, 513, A52
Schweizer, F. 1979, ApJ, 233, 23
Sinnott, B., Hou, A., Anderson, R., Harris, W. E., & Woodley, K. A. 2010, AJ, 140, 2101
Sommer-Larsen, J., Romeo, A. D., & Portinari, L. 2005, MNRAS, 357, 478
Spitler, L. R., & Forbes, D. A. 2009, MNRAS, 392, L1
Springel, V., White, S. D. M., Jenkins, A., et al. 2005, Natur, 435, 629
Stanghellini, L., González-García, A. C., & Manchado, A. 2006, ApJ, 644, 843
Strader, J., Romanowsky, A. J., Brodie, J. P., et al. 2011, ApJS, 197, 33
Tamura, N., Sharples, R. M., Arimoto, N., et al. 2006a, MNRAS, 373, 588
Tamura, N., Sharples, R. M., Arimoto, N., et al. 2006b, MNRAS, 373, 601
Tonry, J. L., Dressler, A., Blakeslee, J. P., et al. 2001, ApJ, 546, 681
van den Bergh, S. 1956, PASP, 68, 449
van den Bergh, S. 1958, Obs, 78, 85
Vanderbeke, J., West, M. J., De Propris, R., et al. 2014, MNRAS, 437, 1734
Waters, C. Z., Zepf, S. E., Lauer, T. R., & Baltz, E. A. 2009, ApJ, 693, 463
West, M. J., & Blakeslee, J. P. 2000, ApJL, 543, L27
West, M. J., Cote, P., Jones, C., Forman, W., & Marzke, R. O. 1995, ApJL, 453, L77
West, M. J., Côté, P., Marzke, R. O., & Jordán, A. 2004, Natur, 427, 31
West, M. J., Jordán, A., Blakeslee, J. P., et al. 2011, A&A, 528, A115
White, R. E., III. 1987, MNRAS, 227, 185
Williams, B. F., Ciardullo, R., Durrell, P. R., et al. 2007a, ApJ, 656, 756
Williams, B. F., Ciardullo, R., Durrell, P. R., et al. 2007b, ApJ, 654, 835
Willman, B., Governato, F., Wadsley, J., & Quinn, T. 2004, MNRAS, 355, 159
Yahagi, H., & Bekki, K. 2005, MNRAS, 364, L86
Yoon, S.-J., Lee, S.-Y., Blakeslee, J. P., et al. 2011, ApJ, 743, 150
York, D. G., Adelman, J., Anderson, J. E., Jr., et al. 2000, AJ, 120, 157
Zhu, L., Long, R. J., Mao, S., et al. 2014, ApJ, 792, 59
Zibetti, S., White, S. D. M., Schneider, D. P., & Brinkmann, J. 2005, MNRAS, 358, 949